PCCP

Carbon dioxide reduction on Ir(111): stable hydrocarbon surface species at near-ambient pressure

Journal:	*Physical Chemistry Chemical Physics*
Manuscript ID	CP-ART-12-2015-007906.R1
Article Type:	Paper
Date Submitted by the Author:	n/a

Complete List of Authors:	Corva, Manuel; University of Trieste, Physics Department; IOM-CNR Laboratorio Tasc Feng, Zhijing; University of Trieste, Physics Department; IOM-CNR Laboratorio Tasc Dri, Carlo; University of Trieste, Department of Physics; IOM-CNR TASC Laboratory, Salvador, Federico; IOM-CNR Laboratorio Tasc Bertoch, Paolo; IOM-CNR Laboratorio Tasc Comelli, Giovanni; University of Trieste, Physics Department; IOM-CNR Laboratorio Tasc Vesselli, Erik; University of Trieste, Physics Department; IOM-CNR Laboratorio Tasc

PCCP Guidelines for Referees

Physical Chemistry Chemical Physics **(*PCCP*) is a high quality journal with a large international readership from many communities**

Only very important, insightful and high-quality work should be recommended for publication in *PCCP*.

To be accepted in *PCCP* - a manuscript must report:

- Very high quality, reproducible new work
- **Important new physical insights** of significant general interest
- A novel, stand-alone contribution

Routine or incremental work should not be recommended for publication. Purely synthetic work is not suitable for PCCP

If you rate the article as 'routine' yet recommend acceptance, please give specific reasons in your report.

Less than 50% of articles sent for peer review are recommended for publication in *PCCP*. The current PCCP Impact Factor is **4.5**.

PCCP is proud to be a leading journal. We thank you very much for your help in evaluating this manuscript. Your advice as a referee is greatly appreciated.

With our best wishes,

Anna Simpson (pccp@rsc.org)
Managing Editor, PCCP

Prof Seong Keun Kim
Chair, PCCP Editorial Board

General Guidance (For further details, see the RSC's Refereeing Procedure and Policy)

Referees have the responsibility to treat the manuscript as confidential. Please be aware of our **Ethical Guidelines** which contain full information on the responsibilities of referees and authors.

When preparing your report, please:
• Comment on the originality, importance, impact and scientific reliability of the work;
• State clearly whether you would like to see the paper accepted or rejected and give detailed comments (with references) that will both help the Editor to make a decision on the paper and the authors to improve it;

Please inform the Editor if:
• There is a conflict of interest;
• There is a significant part of the work which you cannot referee with confidence;
• If the work, or a significant part of the work, has previously been published, including online publication, or if the work represents part of an unduly fragmented investigation.

When submitting your report, please:
• Provide your report rapidly and within the specified deadline, or inform the Editor immediately if you cannot do so. We welcome suggestions of alternative referees.

Carbon dioxide reduction on Ir(111): stable hydrocarbon surface species at near-ambient pressure†

Manuel Corva,[ab] Zhijing Feng,[ab] Carlo Dri,[ab] Federico Salvador,[b] Paolo Bertoch,[b] Giovanni Comelli,[ab] and Erik Vesselli[ab]*

[a]Physics Department, University of Trieste, via Valerio 2, I-34127 Trieste, Italy
[b]IOM-CNR Laboratorio TASC, Area Science Park, S.S. 14 km 163.5, I-34149 Basovizza (Trieste), Italy
*E-mail: vesselli@iom.cnr.it
†Electronic supplementary information (ESI) available. See DOI:

Stable hydrocarbon surface species in the carbon dioxide hydrogenation reaction on Ir(111) were identified by means of infrared-visible sum-frequency generation vibrational spectroscopy and X-ray photoelectron spectroscopy at near-ambient pressure conditions (0.1 mbar). Introducing gas phase binary and ternary mixtures of CO_2, CO, and H_2 into the reaction chamber, stable ethylidyne and ethynyl species were found at the metal surface above 425 K, in remarkable analogy with what observed during the ethylene decomposition process yielding graphene. In addition, for increasing temperature (up to 600 K depending on the reaction conditions), vibrational and electronic spectroscopic fingerprints appeared that could be attributed to the nucleation of aromatic hydrocarbons at the edge of metastable graphenic clusters interacting with the metal surface.

1 Introduction

The catalytic reduction of carbon dioxide to generate useful chemicals like *e.g.* methanol, urea, formic acid, and dimethylcarbonate is a possible route to handle and recycle at least a part of this

waste gas, in order to deal with greenhouse emissions produced by the massive use of fossil fuels.[1–4] Many approaches are investigated, involving both homo- and hetero-geneous catalytic environments, electro-catalytic systems, and solar energy harvesting devices, with a particular effort in the quest for catalysts able to mimic the photosynthetic organic synthesis processes driven in nature by visible light.[2,5] In particular, Ir has recently been considered for the catalytic hydrogenation of carbon dioxide in pincer complexes in aqueous solutions, yielding unprecedented turnover numbers towards the synthesis of formic acid via a formate surface species.[3] Moving to model systems and to atomic-level insight, the Ir(111) termination has been largely investigated in Ultra-High Vacuum (UHV) due to its catalytic activity towards the sequential dehydrogenation of hydrocarbons, with particular focus on acetylene and ethylene.[6–9] A progressive carbon networking process occurs, yielding the formation of a well-ordered, almost perfect and free-standing graphene sheet.[10–12] Stable surface species in the hydrocarbon dehydrogenation process have been identified with both vibrational and electronic spectroscopies under UHV conditions, depending on the reaction temperature. In particular, for increasing temperature, ethylidene ($CHCH_3$), ethylidyne (CCH_3), and ethynyl (CCH) species have been observed, the latter being stable up to the complete dehydrogenation of the surface, occurring above 700 K.[6–9] Analogously, formate, methoxy, and acetate stable surface species are detected upon ethanol and methanol thermal decomposition.[13,14] In this framework, however, insight at reaction conditions closer to ambient pressure is still lacking due to the well-known instrumental pressure gap. In addition, almost no information is available about the interaction of carbon dioxide with Ir due to the low molecule-Ir interaction energy,[4] at variance with other metals like Ni that can activate CO_2 through a consistent charge transfer.[15,16] Recent studies on the Ni(110) surface under near-ambient pressure (NAP) reaction conditions have unveiled important

mechanisms involved in the carbon dioxide reduction process, yielding insight into the role of the surface oxidation state and of graphene and carbide domains.[17] When reacting with hydrogen, CO_2 is found to convert to a stable bi-dentate formate species,[4,18] while other more energetically convenient pathways involve an unstable hydrocarboxyl intermediate.[19] To our knowledge, there is no analogous data available about the carbon dioxide activation and reduction process on iridium surfaces, aiming at identifying stable intermediates and possible reaction pathways, either under UHV or at pressures closer to applicative conditions.[4] On the (110) termination of iridium, CO_2 is indeed only weekly bound in a physisorbed state in UHV and readily desorbs when produced by the reaction of carbon monoxide with pre-adsorbed oxygen.[4,20] Motivated by the above considerations, we present here the results obtained at 10^{-1} mbar by coupling Near-Ambient Pressure X-ray Photoelectron Spectroscopy (NAP-XPS) with the powerful approach of Infrared-Visible Sum-Frequency Generation (IR-Vis SFG) vibrational spectroscopy. The latter technique is indeed intrinsically sensitive to interfaces and allows bridging the pressure gap issues, thus providing insight into the catalyst's surface during the reaction with the gas phase.[21,22] Data were collected with the aim of investigating the interaction of carbon monoxide, carbon dioxide, and hydrogen with the Ir(111) single crystal termination as a function of temperature *in situ* and *in operando* conditions. Repeated measurements were performed, starting each time from a clean Ir surface, in order to ensure reproducibility. Thanks to a comparison of the spectroscopic results with previous literature data, we are able to identify stable hydrocarbon species, remarkably including the ethylidene and ethynyl molecules also present during the acetylene and ethylene dehydrogenation processes.

2 Methods

2.1 SFG Experiments.

A novel experimental setup to study catalytically active heterogeneous phases *in situ* and *in operando*, exploiting IR-Vis SFG,[23] has been commissioned at the Physics Department of the University of Trieste. An UHV preparation chamber (base pressure 5×10^{-11} mbar) equipped with standard sample preparation and characterization instruments (sample fast entry-lock, ion gun, LEED optics, gas line, evaporator, and quartz micro-balance for the deposition of molecules, metallic clusters, and thin film growth) is directly connected to a high-pressure cell, where the sample can be transferred without breaking the vacuum. The sample is held by Ta wires and can be resistively heated up to 1300 K in vacuum and up to 800 K in the reactor (K-type thermocouple). The reactor is equipped with a gas handling system in order to control the pressure of the reactants within the 10^{-10}-10^{+3} mbar range. The inlet of the infrared and visible beams, as well as the outlet of the SFG signal, is provided by UHV-compatible BaF_2 windows. The excitation source of the SFG spectrometer (EKSPLA PL2231) consists in a Nd:YAG, diode pumped picosecond IR laser (λ = 1064 nm, E_{max}/pulse = 25 mJ, repetition rate 50 Hz, pulse duration ~30 ps). The radiation enters a harmonics unit where two visible beams (532 nm) are generated (EKSPLA H500 SFG) by means of non-linear crystals (KD_2PO_4). One of the two beams is then mixed with the remaining fraction of the original IR beam in the parametric generator and difference frequency generator unit (EKSPLA PG501/DFG1P, BBO and $AgGaS_2$ crystals) to yield the tunable IR radiation in the 1000-4500 cm^{-1} range with a spectral width better than 6 cm^{-1}. The whole tunable IR laser beam path length is pressurized with N_2 in order to avoid air absorption. The second visible (532 nm) beam is instead directly delivered to the sample surface. The maximum achievable power at the sample is about 30 and 7 MW for the visible and IR beams (pulse energies of about 1 mJ and 200 μJ, respectively). Both incident

beams are linearly polarized (s or p) with 100:1 purity. Moreover, the polarization of the SFG beam can be selected before entering the monochromator (MS2001) and photomultiplier tube (Hamamatsu R7899) detection system. Both data acquisition and instrument control are performed remotely via software interfaces mainly developed in house. In the present study all spectra were collected in the p-p-p polarization configuration (SFG-visible-infrared), at incidence angles of 55° (IR) and 60° (Vis) from the normal to the surface. The dependence of the SFG signal on the azimuthal angle of the Ir(111) surface was not investigated.

The sample was an 8 mm diameter Ir disc (MaTecK GmbH) of 99.99% purity, with <0.1° orientation accuracy and <0.03 μm roughness. For each experiment, the Ir(111) surface was cleaned by standard cycles of Ar^+ sputtering and annealing in UHV, alternated to oxidation cycles ($p = 10^{-7}$ mbar) to remove residual carbon. Surface order was finally checked by LEED, yielding a sharp (1×1) pattern with extremely low background. SFG spectra acquisition time was about 5 min for the C-O and about 45 min for the C-H stretching regions. High-purity reaction gases (3.0 CO, 4.8 CO_2, 5.5 H_2) where injected into the measurement cell through leak valves from aluminum bottles. The background residual pressure was in the low 10^{-10} mbar range.

2.2 Analysis and interpretation of SFG data.

After normalization to the impinging visible and IR intensities, and to the non-resonant background in order to account for sample alignment issues, SFG spectra were analyzed by least-square fitting methods according to the following widely used parametric, effective expression of the non-linear second order susceptibility,[24–27] explicitly accounting for the IR resonances of the IR-Vis transitions and for the non-resonant background:

$$\frac{I_{SFG}(\omega_{IR})}{I_{vis}I_{IR}(\omega_{IR})} \sim \left|\chi^{(2)}\right|^2 = \left|\chi^{(2)}_{NRes} + \chi^{(2)}_{Res}\right|^2 = \left|A_{NRes}e^{i\varphi_{NR}} + \sum_k \frac{A_k e^{i\varphi_k}}{\omega_{IR}-\omega_k+i\Gamma_k}\right|^2 = \left|e^{i\varphi_{NR}}\right|^2 \left|A_{NRes} + \sum_k \frac{A_k e^{i(\varphi_k-\varphi_{NR})}}{\omega_{IR}-\omega_k+i\Gamma_k}\right|^2 = \left|A_{NRes} + \sum_k \frac{A_k e^{i\Delta\varphi_k}}{\omega_{IR}-\omega_k+i\Gamma_k}\right|^2 \qquad \text{(Eq.1)}$$

In this expression A_{NRes} and A_k are therefore real positive numbers and account for the amplitudes of the non-resonant and k^{th}-resonant contributions, respectively, $\Delta\varphi_k=\varphi_k-\varphi_{NR}$ is the phase difference between the k^{th}-resonance and the non-resonant background, ω_k is the energy of the k^{th}-resonance, and Γ_k its Lorentzian broadening related to the resonance lifetime. In order to account for inhomogeneity broadening, in specific cases the resonant part of the lineshape was convoluted with a Gaussian envelope.[28–30] According to previous literature, the Gaussian contribution to the lineshape is easily resolved only if it is comparable with the Lorentzian width. In the specific cases where the latter is predominant, the inhomogeneity contribution is hardly obtained from the fitting procedure and can be neglected to a good approximation.[29] A very detailed and careful analysis of the complex IR-Vis spectra in the C-H region was performed in order to obtain a reliable separation of the different contributions originating from adsorbed species. This was achieved by identifying a unique set of lineshape parameters that allowed optimal fitting of the whole data set. For each SFG spectrum throughout the manuscript we plot the normalized SFG intensity (dots) together with the corresponding best fit (grey lines) according to the above intensity function (Eq. 1), and with the corresponding intensity deconvolution (colors) accounting for the interference of each of the resonances with the non-resonant background. A very detailed description of the SFG data analysis and of the plotted quantities can be found in the Supplementary Information, together with a complete set of best fitting parameters of the full SFG data set.

2.3 NAP-XPS Experiments.

NAP (mbar range) XPS measurements were carried out at the ISISS end-station of the Bessy synchrotron radiation facility at the Helmholtz Zentrum Berlin (Germany).[31] The same Ir(111) single crystal used in the SFG experiments was mounted on a sapphire holder by means of Ta supports and screws. Temperature was measured with a K-type thermocouple, and the sample was heated by laser irradiation of its unpolished back face. After each reactivity experiment, the Ir(111) surface was cleaned by standard cycles of ion sputtering (2.5 keV, Ar^+) and annealing in high vacuum to 750°C, the highest attainable temperature on the sample holder. Absence of contaminants was verified by measuring both selected XPS regions (*e.g.* C 1*s*, O 1*s*) and overview spectra. The flux and pressure of the gases introduced into the reaction cell were handled by means of mass-flow controllers and a motorized valve. The effective partial pressure of the reactants in the measurement chamber may have differed with respect to the nominal values due to the different pumping speeds of different molecules. The ratios we report are therefore target set point values only. Gas purity (always better than 3.0) was checked and monitored using a quadrupole mass spectrometer. The residual background pressure in the measurement chamber was in the 10^{-7} mbar range. Adsorption of the single reactants on the clean Ir(111) surface was performed to exclude effects due to residual contaminants. Absence of the latter was confirmed by means of XPS. NAP-XPS spectra were collected in normal emission geometry and binding energies were calibrated with respect to the Fermi level for each oxygen ($h\nu$ = 650 eV) and carbon ($h\nu$ = 400 eV) core level spectrum, yielding an accuracy in the determination of the binding energy values of ±0.1 eV. After normalization and subtraction of a Shirley background,[32] spectra were analyzed by least-square fitting of the data with Doniach-Šunjić profiles,[33] convoluted with a Gaussian envelope to account for experimental resolution,

inhomogeneity and thermal broadening. A very detailed and careful analysis of the C and O 1*s* core level spectra was performed in order to disentangle the contributions originating from different species. This was achieved by identifying a single set of lineshape parameters that allowed optimal fitting of all the C or O 1*s* spectra. Within this set, in order to reduce the number of degrees of freedom, identical lineshapes were used for groups of similar species. In particular, C 1*s* spectra were fitted with distinct lineshapes for CO, and for C-C and C-H species. The resulting binding energy values were assigned on the basis of literature data as reported in the text.

3 Results and discussion

3.1 CO_2 and CO adsorption.

In order to identify the spectroscopic features related to carbon dioxide adsorption and dissociation, the Ir(111) surface was exposed to 10^{-1} mbar CO_2. In Figure 1 (left panel), IR-Vis SFG spectra of the C-O stretching region collected at selected temperature values are shown. Two distinct features are clearly visible, shifting with temperature from 2080 to 2060 cm^{-1} and from 2070 to 2050 cm^{-1}. The data fitting procedure yields constant phases relative to the non-resonant background of 32° and 37°, respectively. At the highest investigated temperature (575 K), only one feature is present at low energy (2024 cm^{-1}). Details about the SFG fitting parameters of the whole data set can be found in the Supplementary Information (Tables S1-3). In Figure 1 (right panel) we report for comparison also the data obtained upon exposure of the surface to CO under the same experimental conditions. Only one feature is visible in the IR-Vis SFG spectra, shifting progressively for increasing temperature from 2079 to 2063 cm^{-1} and with the same lineshape of the corresponding peak (light green) in the carbon dioxide experiment. The Gaussian broadening is larger with respect to the CO_2 case, reaching values up to 7.7 cm^{-1}. As

for CO_2, also in this case a single, broader feature is found at 575 K, at slightly lower energy (2016 cm^{-1}). We remind that due to the physical origin of the SFG signal, intensities are not necessarily related to surface concentration of the adspecies. Therefore, no conclusions about the surface coverage can be drawn.

On the basis of literature data, it is known that CO adsorption on Ir(111) is non-dissociative at room temperature, yielding a saturation coverage of 0.7 ML (monolayer) with CO molecules adsorbed at on-top Ir sites in a $(3\sqrt{3}\times3\sqrt{3})R30°$-19CO structure. The geometric arrangement of the adsorbed CO molecules is best described within the framework of a Frenkel-Kontorova model, yielding a progressive deviation of the C-O molecular axis from the surface normal with the distance from the center of the CO islands.[34,35] For instance, this nicely accounts for the inhomogeneous broadening observed in our IR-Vis SFG spectra. We further confirm this picture by means of NAP-XPS O and C 1*s* core level spectra collected at 375 K (Figure 2, top panels): apart from small amounts of carbon phases (284 eV) and atomic oxygen (529.9 eV) most likely due to dissociation at surface defects, a single CO species can be observed, yielding spectroscopic peaks at 532.0 and 286.1 eV for the O and C 1*s* core levels, respectively, corresponding to on-top adsorption, in agreement with the literature.[34]

In the case of dissociative adsorption of CO_2, the core level binding energies associated to CO (Figure 2, bottom panel) show a consistent shift to 530.9 eV (O 1*s*) and 286.9 eV (C 1*s*), while an intense feature associated to atomic oxygen appears (529.6 eV, cyan). Complete dissociation is possible, evident from the accumulation of carbon (283.9 eV, red). The reaction $CO_2 \rightarrow CO+O \rightarrow C+2O$ is in agreement with the literature, since carbon monoxide decomposition on Ir(111) is promoted by co-adsorbed oxygen.[36] Above 600 K (not shown), the Ir surface remains oxygen-covered since CO desorbs, while carbon is oxidized and therefore removed.

Only a single sharp peak remains visible at 529.9 eV and no feature is detected in the C 1*s* region. In the vibrational spectra, besides the main C-O stretching peak, a low energy shoulder appears (Figure 1, left panel, dark green). We therefore ascribe the two contributions to CO in on-top configuration (2080-2060 cm^{-1}) and to CO in a modified terminal Ir site close to adsorbed atomic oxygen (2070-2050 cm^{-1}), respectively.[35]

3.2 CO_2 reduction.

The Ir(111) sample was exposed to different reactants mixtures to investigate both the carbon dioxide hydrogenation process and the role of carbon monoxide at a total pressure of 10^{-1} mbar. In Figure 3, IR-Vis SFG spectra in the C-O stretching region are reported for selected relative concentrations of the reactants, going from a pure CO/H_2 (left) to a pure CO_2/H_2 (right) environment. The spectra reveal the presence of CO adsorbed in on-top configuration, with a desorption temperature that is progressively decreasing when raising the CO_2 partial pressure. For a pure CO/H_2 mixture a single feature dominates (light green, left), while a lower energy shoulder (dark green) appears at high temperature in analogy to the pure CO_2 case. When adding CO_2, instead, the peak at low energy is already present at room temperature, indicating an influence of co-adsorbates on adsorbed CO.

Moving to the C-H stretching modes (Figure 4), an interesting set of vibrational features appears, indicating the presence of stable adsorbed hydrocarbon species. For the sake of completeness, a broader range of $CO_2/CO/H_2$ concentration ratios has been investigated (not shown), providing no significant additional insight. The full set of IR-Vis SFG data in the C-H stretching region and the details about the fitting parameters are reported in the Supplementary Information. The data shown in the figure immediately indicate that, when carbon monoxide is

present in the gas mixture of the reactants, hydrocarbon surface species develop at higher temperature. At the lowest investigated H_2/CO_2 ratio (H_2/CO_2 = 3, not shown), C-H bonds can be detected already at 425 K. Deeper insight can be obtained by least-square fitting of the data, as discussed in the following. Starting from the low energy side of the spectra, a feature with very low intensity (yellow) can be identified at 2845 cm^{-1} with a phase of 185°. A more intense peak (dark red) is present at 2904 cm^{-1} (phase -20°/+15°), showing a precise trend as a function of temperature and carbon dioxide concentration: its intensity is indeed higher at low temperature and for high carbon dioxide partial pressures. A very intense and broad feature develops at 2976 cm^{-1} (light red, phase 265°) and other three peaks (different blue grades) appear at 3000, 3035, and 3078 cm^{-1} (phases 240°, 68°, and 107°, respectively). We observe that at first glance a single resonance in phase-quadrature with respect to the non-resonant background, i.e. with a dispersive Fano-like lineshape, may already correctly reproduce the experimental data, instead of the two peaks at 3000 and 3035 cm^{-1} (cyan and light blue in Figure 4), in analogy to the case of the feature at 2904 cm^{-1} (dark red). However, this is not adequate, yielding only poor chi-values and structured residuals in the least-square fitting analysis. A thorough discussion of this issue is presented in the Supplementary Information. At variance with the C-O modes, we do not observe a significant shift of the resonances as a function of the surface temperature. Interestingly, the intensity of the feature at 3078 cm^{-1} grows with temperature at the expense of the intensity of the peak at 3035 cm^{-1}.

NAP-XPS core level spectra collected under the same reaction conditions in the O 1*s* region (not shown) reveal only the presence of adsorbed carbon monoxide, depending on the reaction temperature, while other oxygen-containing species, including atomic oxygen, if present, are below the detection limit. Instead, several spectral contributions appear in the C 1*s*

region (Figure 5). In addition to the peak assigned to carbon monoxide (286.1 eV, green), other peaks appear at lower binding energy, specifically at 283.0, 283.4, 283.9, 284.3, and 284.7 eV. Interestingly and in agreement with what observed with IR-Vis SFG, there is a site competition effect, so that the higher the CO coverage (bottom left part of the graph), the lower the intensities of these contributions, apart from the spectrum at 600 K in pure CO_2/H_2 (top right) where almost no carbon signal is present.

3.3 Identification of stable surface species.

For clarity, the energy positions of the resolved spectroscopic features are reported in Tables 1 and 2 for the vibrational and electronic probes, respectively, together with reference literature data supporting the assignments discussed in the following. The identification of carbon monoxide, originated by both adsorption from the gas phase and/or from the dissociation of carbon dioxide, depending on the reaction conditions, is straightforward when comparing vibrational (peaks at 2013-2083 cm^{-1}) and electronic (peak at 286.1 eV) spectroscopy data with previous literature (Tables 1 and 2, respectively) and with our benchmark experiments (Figures 1 and 2).

Instead, much more effort is needed to interpret and assign the remaining spectroscopic fingerprints. We start from the vibrational features at 2904 and 2976 cm^{-1} (red peaks in Figure 4). On the basis of previous literature data on palladium,[37] iridium,[7] and platinum surfaces,[38,39] the two resonances may be associated with the symmetric and asymmetric stretching modes of the methyl groups of ethylidyne (CCH_3). Indeed, also in the XPS C 1*s* core level spectra the triplet at 283.4, 283.9, and 284.3 eV (Figure 5, red-yellow) well compares with literature data of ethylidyne on Ir(111) obtained from the thermal decomposition of ethylene.[9] The former two peaks are attributed to the two non-equivalent carbon atoms of the molecule, which is bonded to

the surface in upright position through the dehydrogenated termination, while the latter C 1*s* peak is ascribed to the vibrational excitation of the methyl group. To obtain an independent proof of this interpretation, we studied by means of IR-Vis SFG spectroscopy the ethylene dissociation process. In UHV and at temperatures between 300 and 450 K, only two features are clearly visible in the C-H stretching region at 2880 and 2975 cm^{-1}, where, as known from the literature,[9] only ethylidyne is present as a product of the stepwise decomposition of ethylene into ethylidene, ethylidyne, and finally ethynyl species. This further supports our interpretation. By directly comparing the CO_2+CO+H_2 reaction data with the ethylene decomposition experiments on Ir(111) and on the basis of SFG and Fourier Transform Infra-Red (FTIR) measurements on a Pt(111) surface,[40,41] the small peak that we observe at 2845 cm^{-1} (Figure 4, yellow) may be ascribed to the asymmetric CH_3 bend in Fermi resonance with the symmetric C-H stretch.[41] We also observe that if the C-CH_3 bond were perpendicular to the surface, the asymmetric stretch mode would not be visible. This accounts for the poor intensity observed in the spectra obtained upon decomposition of the ethylene layer at variance with the case of the CO_2+CO+H_2 reaction. The intense contribution of this mode to the IR-Vis SFG spectra of the reaction is therefore associated with a deviation of the molecular axis from the upright position due to co-adsorption effects. An alternative, but less supported interpretation of the SFG peak at 2845 cm^{-1} is to assign it to other unsaturated carbon species, namely CH_x, in association with the spectroscopic feature at 283.0 eV in the C 1*s* spectra.[13]

Upon annealing of an ethylidyne layer on Ir(111) above 400 K, dehydrogenation occurs, yielding formation of two non-equivalent ethynyl (CCH) species contributing at 3002 and 3023 cm^{-1} in the vibrational spectra and showing peaks at 283.25 and 283.56 eV in the C 1*s* core level spectra.[9] We therefore attribute to these species the peaks showing up in the reduction

experiments at 3000 and 3035 cm^{-1} (Figure 4, light and intermediate blue). This agrees with the necessity of introducing into the fit procedure two resonances with almost opposite phase, rather than a single dispersive resonance. The phase difference suggests two distinct non-equivalent adsorption geometries for the molecule. Concerning the XPS spectra instead (Figure 5), ethynyl is expected to contribute to the peak at 283.4 eV and is therefore not distinctly resolved in this case.

Finally, with increasing temperature and carbon dioxide concentration (Figure 4, dark blue), a broad feature appears as a depression at 3078 cm^{-1} and is associated with the contribution at 284.7 eV (Figure 5, dark blue) in the C 1*s* core level spectra. While the latter is ascribed to the nucleation of carbide and graphene clusters strongly interacting with the metal surface,[12,42] the vibrational feature, typical of a C-H stretching mode, appears at an energy that is characteristic of aromatic hydrocarbon species.[43] This is compatible with the progressive formation of carbon links, *i.e.* the initial step of a graphene networking process assisted by hydrogen at the periphery of the nucleation islands in agreement with the literature.[44] Further dehydrogenation would therefore yield to the formation of graphenic domes and nucleation islands.[12] However, for the highest studied temperature (600 K) and in absence of carbon monoxide, the high partial pressure of hydrogen in the reaction environment leads to the almost complete reduction and removal of surface carbon (upper right spectrum in Figure 5).

The above findings put in light two significant results. It is indeed observed that stable ethylidyne species can be obtained by a catalytic hydrogenation process at the Ir surface, thus obtaining the same precursor to graphene growth that is generally formed upon thermal decomposition of ethylene adsorbed from the gas phase under UHV conditions. Secondly, the consequent growth of graphene is found to occur via a carbon networking process related with a

progressive formation and dehydrogenation of aromatic species, possibly at the border of the graphene domes. Our work represents therefore a possible spectroscopic evidence and confirmation for what was very recently observed by means of microscopy experiments on both Ir and Ni single crystal surfaces when growing graphene from thermal decomposition of hydrocarbons.[44,45] An important role in the whole reaction mechanism is most likely played by surface and/or subsurface atomic hydrogen species,[46] obtained upon dissociation of gas phase molecular hydrogen from the reactants' background. Our methods did not allow the detection of these species, but, on the basis of literature data obtained under UHV conditions,[47] it is known that atomic hydrogen is still present on the surface up to 450 K on Ir(111). By means of a cartoon representation, we summarize for the sake of clarity in Figure 6 the adsorbed chemical species that we were able to identify at the Ir(111) surface.

4 Conclusions

In conclusion, stable hydrocarbon surface species in the carbon dioxide hydrogenation reaction on Ir(111) were identified by means of infrared-visible sum-frequency generation vibrational spectroscopy and X-ray photoelectron spectroscopy at near-ambient pressure conditions. Ethylidyne and ethynyl species were found at the metal surface above 425 K, in interesting analogy with the ethylene decomposition process yielding graphene. In addition, for increasing temperature (up to 600 K depending on the reaction conditions), vibrational and electronic spectroscopic fingerprints appeared that could be attributed to the nucleation of aromatic hydrocarbons at the periphery of graphenic metastable clusters interacting with the

surface. This provides insight into the graphene growth process that takes place by the progressive extension of graphene islands by means of intermediate aromatic terminations at low temperature.

Acknowledgements

This research was supported by Italian MIUR through the project Futuro in Ricerca FIRB 2010 no. RBFR10J4H7. Consorzio per l'Incremento degli Studi e delle Ricerche dei Dipartimenti di Fisica dell'Università degli Studi di Trieste, Fondazione Casali, and Beneficentia Stiftung are also acknowledged for their contribution in the realization of the SFG setup. Part of the research leading to these results has received funding from the European Community's Seventh Framework Program (FP7/2007-2013) under Grant Agreement No. 226716. We acknowledge the Helmholtz-Zentrum Berlin for provision of synchrotron radiation beamtime at beamline ISISS of BESSY II. The support by Axel Knop-Gericke and Mark Greiner is gratefully acknowledged. Technical support from Andrea Martin (CNR-IOM) and Giovanni Fabian (UniTs), and from the whole administration section of the Physics Department of the University of Trieste is thankfully acknowledged. E.V. thanks K. Föttinger and G. Rupprechter for fruitful discussions about the SFG setup, and N. Seriani for helpful discussions about data interpretation. CNR-IOM is acknowledged for hosting the SFG facility.

REFERENCES

1 C. Song, *Catal. Today*, 2006, **115**, 2–32.

2 C. Wang, Z. Xie, K. E. DeKrafft and W. Lin, *J. Am. Chem. Soc.*, 2011, **133**, 13445–13454.

3 R. Tanaka, M. Yamashita and K. Nozaki, *J. Am. Chem. Soc.*, 2009, **131**, 14168–14169.

4 H.-J. Freund and M. W. Roberts, *Surf. Sci. Rep.*, 1996, **25**, 225–273.

5 J. Barber, *Nat. Struct. Biol.*, 2001, **8**, 577–579.

6 T. S. Marinova and D. V. Chakarov, *Surf. Sci.*, 1987, **192**, 275–282.

7 T. S. Marinova and K. L. Kostov, *Surf. Sci.*, 1987, 181, 573–585.

8 K. L. Kostov and T. S. Marinova, *Surf. Sci.*, 1987, **184**, 359–373.

9 S. Lizzit and A. Baraldi, *Catal. Today*, 2010, **154**, 68–74.

10 B. E. Nieuwenhuys, D. I. Hagen, G. Rovida and G. A. Somorjai, *Surf. Sci.*, 1976, 59, 155–176.

11 J. Wintterlin and M. L. Bocquet, *Surf. Sci.*, 2009, **603**, 1841–1852.

12 P. Lacovig, M. Pozzo, D. Alfè, P. Vilmercati, A. Baraldi and S. Lizzit, *Phys. Rev. Lett.*, 2009, **103**, 166101.

13 C. J. Weststrate, W. Ludwig, J. W. Bakker, A. C. Gluhoi and B. E. Nieuwenhuys, *ChemPhysChem*, 2007, **8**, 932–937.

14 C. J. Weststrate, W. Ludwig, J. W. Bakker, A. C. Gluhoi and B. E. Nieuwenhuys, *J. Phys. Chem. C*, 2007, **111**, 7741–7747.

15 C. Dri, A. Peronio, E. Vesselli, C. Africh, M. Rizzi, A. Baldereschi, M. Peressi and G. Comelli, *Phys. Rev. B*, 2010, **82**, 165403.

16 X. Ding, L. De Rogatis, E. Vesselli, A. Baraldi, G. Comelli, R. Rosei, L. Savio, L. Vattuone, M. Rocca, P. Fornasiero, F. Ancilotto, A. Baldereschi and M. Peressi, *Phys. Rev. B*, 2007, **76**, 195425.

17 E. Monachino, M. Greiner, A. Knop-Gericke, R. Schlögl, C. Dri, E. Vesselli and G. Comelli, *J. Phys. Chem. Lett.*, 2014, **5**, 1929–1934.

18 E. Vesselli, L. De Rogatis, X. Ding, A. Baraldi, L. Savio, L. Vattuone, M. Rocca, P. Fornasiero, M. Peressi, A. Baldereschi, R. Rosei and G. Comelli, *J. Am. Chem. Soc.*, 2008, **130**, 11417–11422.

19 E. Vesselli, M. Rizzi, L. De Rogatis, X. Ding, A. Baraldi, G. Comelli, L. Savio, L. Vattuone, M. Rocca, P. Fornasiero, A. Baldereschi and M. Peressi, *J. Phys. Chem. Lett.*, 2010, **1**, 402–406.

20 T. Matsushima, Y. Ohno and K. Nagai, *Surf. Sci.*, 1990, 239, L561–L564.

21 G. Rupprechter and C. Weilach, *Nano Today*, 2007, 2, 20–29.

22 G. Rupprechter, *Catal. Today*, 2007, **126**, 3–17.

23 Y. R. Shen, *Nature*, 1989, 337, 519–525.

24 B. Busson and A. Tadjeddine, *J. Phys. Chem. C*, 2009, **113**, 21895–21902.

25 F. Vidal and A. Tadjeddine, *Rep. Prog. Phys.*, 2005, **68**, 1095–1127.

26 C. S. Tian and Y. R. Shen, *Surf. Sci. Rep.*, 2014, **69**, 105–131.

27 A. G. Lambert, P. B. Davies and D. J. Neivandt, *Appl. Spectrosc. Rev.*, 2005, **40**, 103–145.

28 J. Y. Huang and Y. R. Shen, *Phys. Rev. A*, 1994, **49**, 3973–3981.

29 L. Velarde and H.-F. Wang, *Phys. Chem. Chem. Phys.*, 2013, **15**, 19970–84.

30 A. L. Mifflin, L. Velarde, J. Ho, B. T. Psciuk, C. F. a. Negre, C. J. Ebben, M. A. Upshur, Z. Lu, B. L. Strick, R. J. Thomson, V. S. Batista, H.-F. Wang and F. M. Geiger, *J. Phys. Chem. A*, 2015, **119**, 1292–1302.

31 A. Knop-Gericke, E. Kleimenov, M. Havecker, R. Blume, D. Teschner, S. Zafeiratos, R. Schlögl, V. Bukhtiyarov, V. V. Kaichev, I. P. Prosvirin, A. Nizovskii, H. Bluhm, A. Barinov, P. Dudin and M. Kiskinova, *Adv. Catal.*, 2009, **52**, 213–272.

32 D. Shirley, *Phys. Rev. B*, 1972, **5**, 4709–4714.

33 S. Doniach and M. Sunjic, *J. Phys. C*, 1970, **3**, 285–291.

34 E. Grånäs, M. Andersen, M. A. Arman, T. Gerber, B. Hammer, J. Schnadt, J. N. Andersen, T. Michely and J. Knudsen, *J. Phys. Chem. C*, 2013, **117**, 16438–16447.

35 J. Lauterbach, R. W. Boyle, M. Schick, W. J. Mitchell, B. Meng and W. H. Weinberg, *Surf. Sci.*, 1996, 366, 228.

36 M. Pan, S. Hoang, J. Gong and C. B. Mullins, *Chem. Commun. (Camb).*, 2009, 7300–7302.

37 M. Morkel, G. Rupprechter and H.-J. Freund, *Surf. Sci.*, 2005, **588**, L209–L219.

38 K. R. McCrea and G. A. Somorjai, *J. Mol. Catal. A Chem.*, 2000, 163, 43–53.

39 R. Deng, E. Herceg and M. Trenary, *Surf. Sci.*, 2004, **573**, 310–319.

40 P. Cremer, C. Stanners, J. W. Niemantsverdriet, Y. R. Shen and G. Somorjai, *Surf. Sci.*, 1995, **328**, 111–118.

41 I. J. Malik, V. K. Agrawal and M. Trenary, *J. Chem. Phys.*, 1988, **89**, 3861–3869.

42 R. Larciprete, S. Fabris, T. Sun, P. Lacovig, A. Baraldi and S. Lizzit, *J. Am. Chem. Soc.*, 2011, **133**, 17315–17321.

43 M. Endlich, S. Gozdzik, N. Néel, A. L. da Rosa, T. Frauenheim, T. O. Wehling and J. Kröger, *J. Chem. Phys.*, 2014, **141**, 184308.

44 L. L. Patera, F. Bianchini, G. Troiano, C. Dri, C. Cepek, M. Peressi, C. Africh and G. Comelli, *Nano Lett.*, 2015, **15**, 56–62.

45 Y. Li, D. Subramaniam, N. Atodiresei, P. Lazić, V. Caciuc, C. Pauly, A. Georgi, C. Busse, M. Liebmann, S. Blügel, M. Pratzer, M. Morgenstern and R. Mazzarello, *Adv. Mater.*, 2013, **25**, 1967–1972.

46 E. Vesselli, J. Schweicher, A. Bundhoo, A. Frennet and N. Kruse, *J. Phys. Chem. C*, 2011, **115**, 1255–1260.

47 D. V. Chakarov and T. S. Marinova, *Surf. Sci.*, 1988, **204**, 147–160.

48 M. Y. Smirnov, V. V. Gorodetskii, A. R. Cholach and D. Y. Zemlyanov, *Surf. Sci.*, 1994,

311, 308–321.

Figures and Tables Captions

Table 1 Energies (cm^{-1}) of the observed vibrational modes, comparison with the literature, and proposed identification of the stable species.

Table 2 C 1*s* core level binding energies (eV), comparison with the literature, and proposed identification of the stable species.

Fig. 1 IR-Vis SFG spectra of Ir(111) in the C-O stretching region collected *in situ* upon exposure of the clean surface to 10^{-1} mbar CO (right panel) and CO_2 (left panel) at selected temperature steps, increasing bottom to top; data (black dots) and the results of the least square fitting (grey curves) are shown; color-filled curves represent deconvoluted intensity modulations with respect to the non-resonant background. [λ_{Vis} = 532 nm; p-p-p polarization]

Fig. 2 NAP-XPS O (left) and C 1*s* (right) core level spectra of Ir(111) collected *in situ* upon exposure of the clean surface to 10^{-1} mbar CO (upper panels) and CO_2 (bottom panels) at 375 K. The deconvolution (color) of the data (black dots) obtained by means of least square fitting (grey curves) is also shown. [hν = 650 (400) eV for oxygen (carbon)]

Fig. 3 IR-Vis SFG spectra of Ir(111) in the C-O stretching region collected *in situ* and *in operando* during the hydrogen reduction of CO (left panel), CO_2 (right panel), and of a mixture of the two (central panel) at a total pressure of 10^{-1} mbar and for progressively increasing temperature (bottom to top); data (black dots) and the results of the least square fitting (grey curves) are shown; color-filled curves represent deconvoluted intensity modulations with respect to the non-resonant background. [λ_{Vis} = 532 nm; p-p-p polarization]

Fig. 4 IR-Vis SFG spectra of Ir(111) in the C-H stretching region collected *in situ* and *in operando* during the hydrogen reduction of CO (left panel), CO_2 (right panel), and of a mixture of the two (central panel) at a total pressure of 10^{-1} mbar and for progressively increasing temperature (from bottom to top); data (black dots) and the results of the least square fitting (grey curves) are shown; color-filled curves represent deconvoluted intensity modulations with respect to the non-resonant background. [λ_{Vis} = 532 nm; p-p-p polarization]

Fig. 5 NAP-XPS C 1*s* core level spectra of Ir(111) during the hydrogen reduction of CO (left panel), CO_2 (right panel), and of a mixture of the two (central panel) at a total pressure of 10^{-1} mbar and for progressively increasing temperature (from bottom to top). The deconvolution (color) of the data (black dots) obtained by means of least square fitting (grey curves) is also shown. [hν =400 eV]

Fig. 6 Cartoon summary of the stable adsorbed species identified at the Ir(111) surface upon hydrogenation of CO and CO_2 at NAP conditions.

Table 1.

This work	Mode	Species	Reference	
2013-2083	C-O stretch	CO (on-top)	2030-2090[35]	Ir
2845	Fermi res.	Ethylidyne (CCH_3)	2795,2857[40,41]	Pt
2904	CH_3 symm. stretch	Ethylidyne (CCH_3)	2870-2890[37,38] 2880*	Pd,Pt Ir
2976	CH_3 asymm. stretch	Ethylidyne (CCH_3)	2940-2960[7,39] 2975*	Ir,Pt
3000,3035	CH stretch	Ethynyl (CCH)	3010-3040[7,39,48] 3002,3023*	Ir,Pt
3078	CH stretch	Aromatic hydrocarbon	3057[43]	Ir

**This work, from ethylene dissociation: see Supplementary Information for details*

Table2.

This work	Species	Reference
283.0	Methylidyne (CH)	283.2[13]
283.4	Ethylidyne (CCH_3)	283.53[9]
	Ethynyl (CCH)	283.25-283.56[9]
283.9	Ethylidyne (CCH_3)	283.93[9]
	Surface carbon	283.77[9]
284.3	Ethylidyne (CCH_3) – vib. exc.	284.32[9]
284.7	Graphene interacting with Ir	284.6[42]
	C atoms at the periphery of graphenic clusters	284.9[12]
286.1	CO	286.2-286.3[14,34]

All literature data refer to the Ir(111) surface

Figure 1.

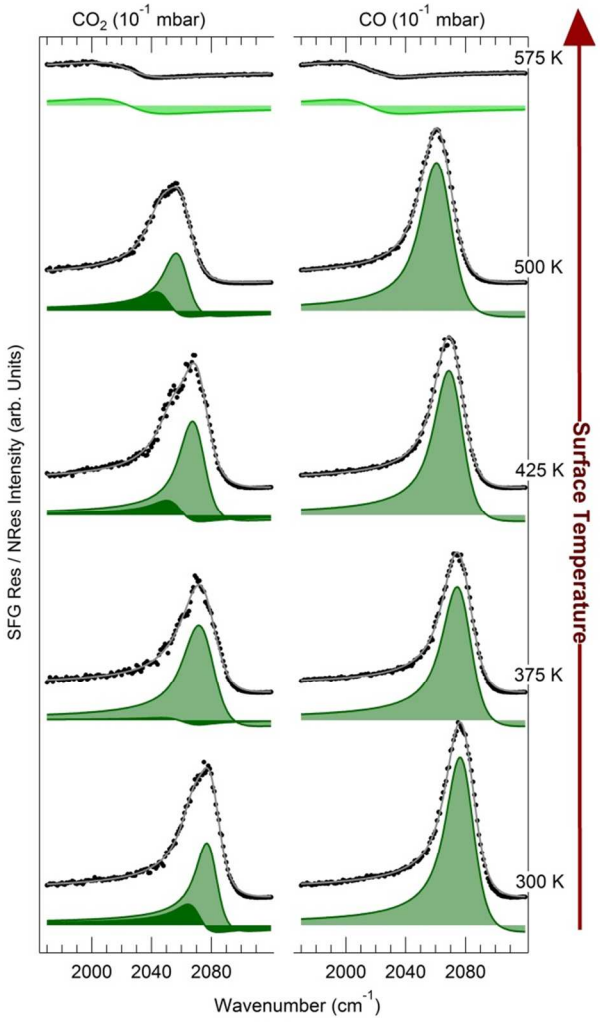
CO2 (10-1 mbar)
CO (10-1 mbar)
575 K
500 K
425 K
375 K
300 K
Surface Temperature
SFG Res / NRes Intensity (arb. Units)
2000 2040 2080
2000 2040 2080
Wavenumber (cm-1)

Figure 2.

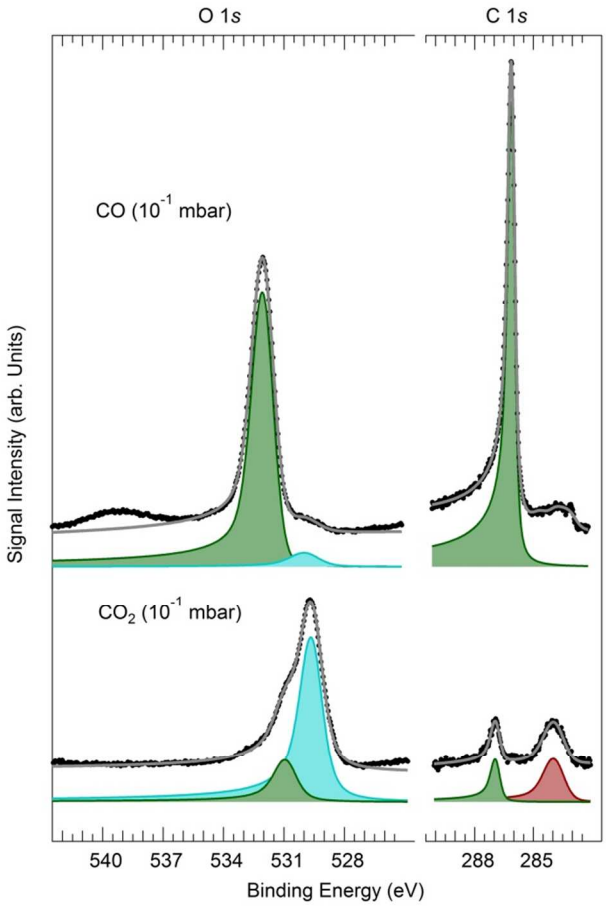
O 1s
C 1s
CO (10^-1 mbar)
CO2 (10^-1 mbar)
Signal Intensity (arb. Units)
540
537
534
531
528
288
285
Binding Energy (eV)

Figure 3.

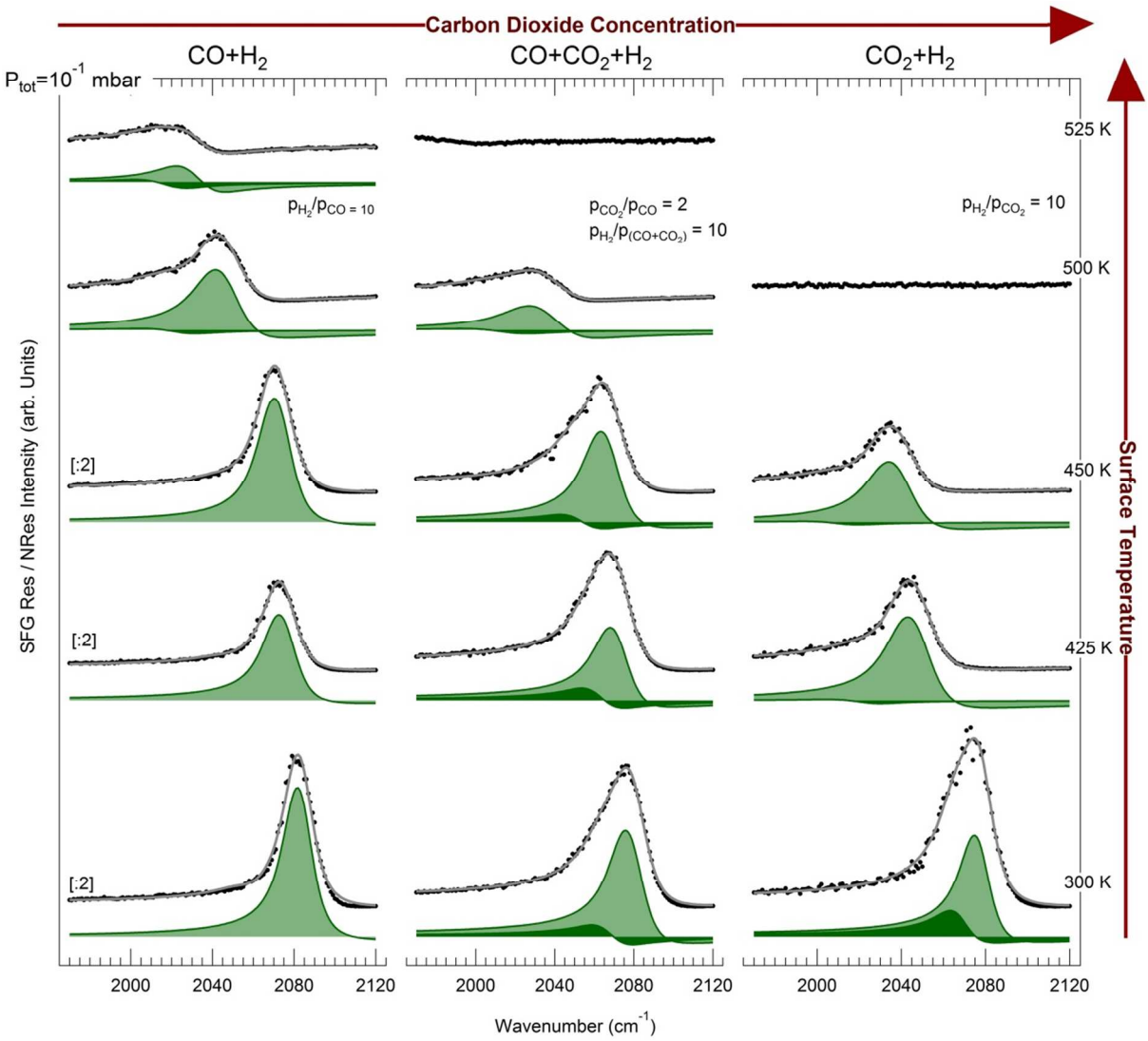
Carbon Dioxide Concentration
CO+H2
CO+CO2+H2
CO2+H2
Ptot=10-1 mbar
525 K
500 K
450 K
425 K
300 K
pH2/pCO = 10
pCO2/pCO = 2
pH2/p(CO+CO2) = 10
pH2/pCO2 = 10
[:2]
[:2]
[:2]
SFG Res / NRes Intensity (arb. Units)
Surface Temperature
2000
2040
2080
2120
Wavenumber (cm-1)

Figure 4.

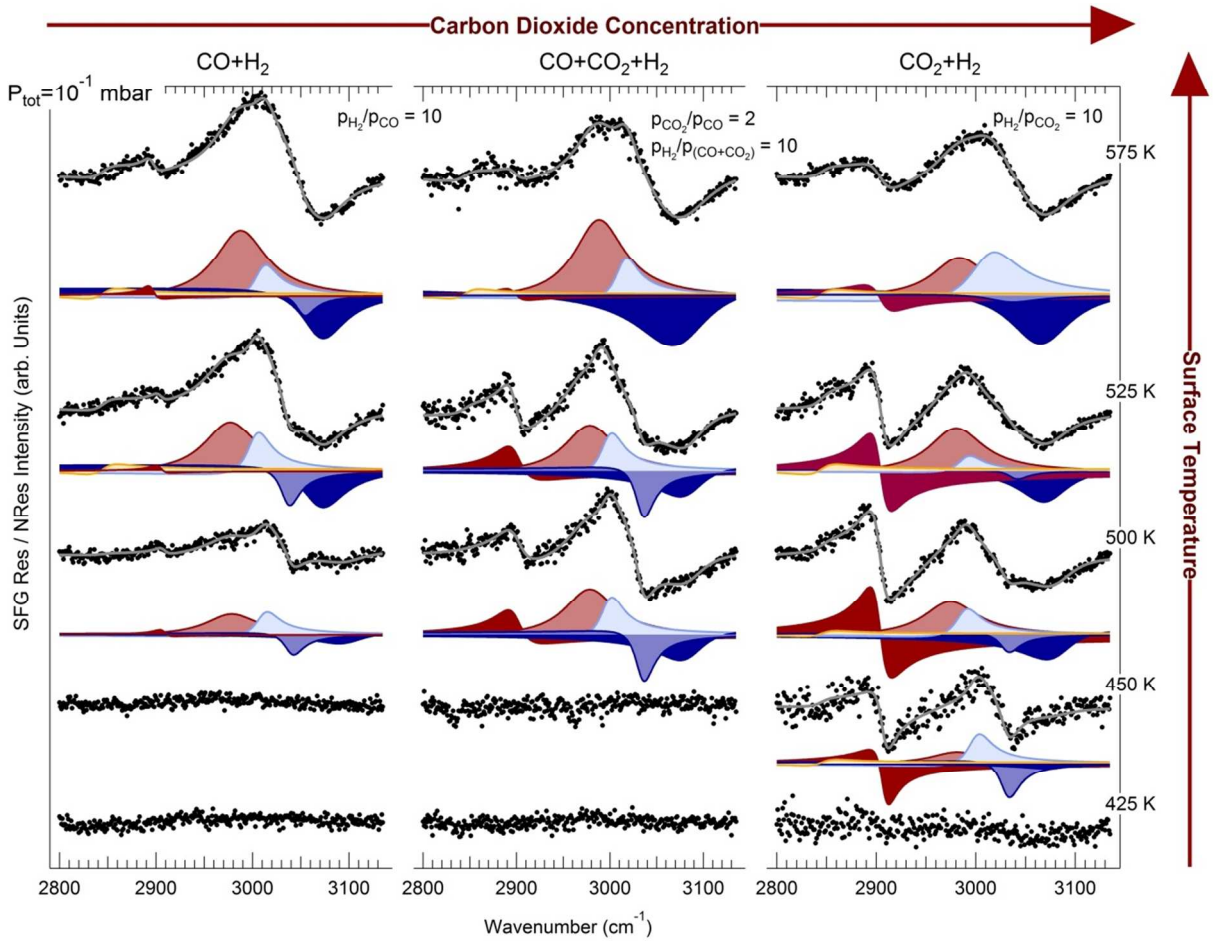
Carbon Dioxide Concentration
CO+H2
CO+CO2+H2
CO2+H2
Ptot=10-1 mbar
pH2/pCO = 10
pCO2/pCO = 2
pH2/p(CO+CO2) = 10
pH2/pCO2 = 10
575 K
525 K
500 K
450 K
425 K
Surface Temperature
SFG Res / NRes Intensity (arb. Units)
2800
2900
3000
3100
Wavenumber (cm-1)

Figure 5.

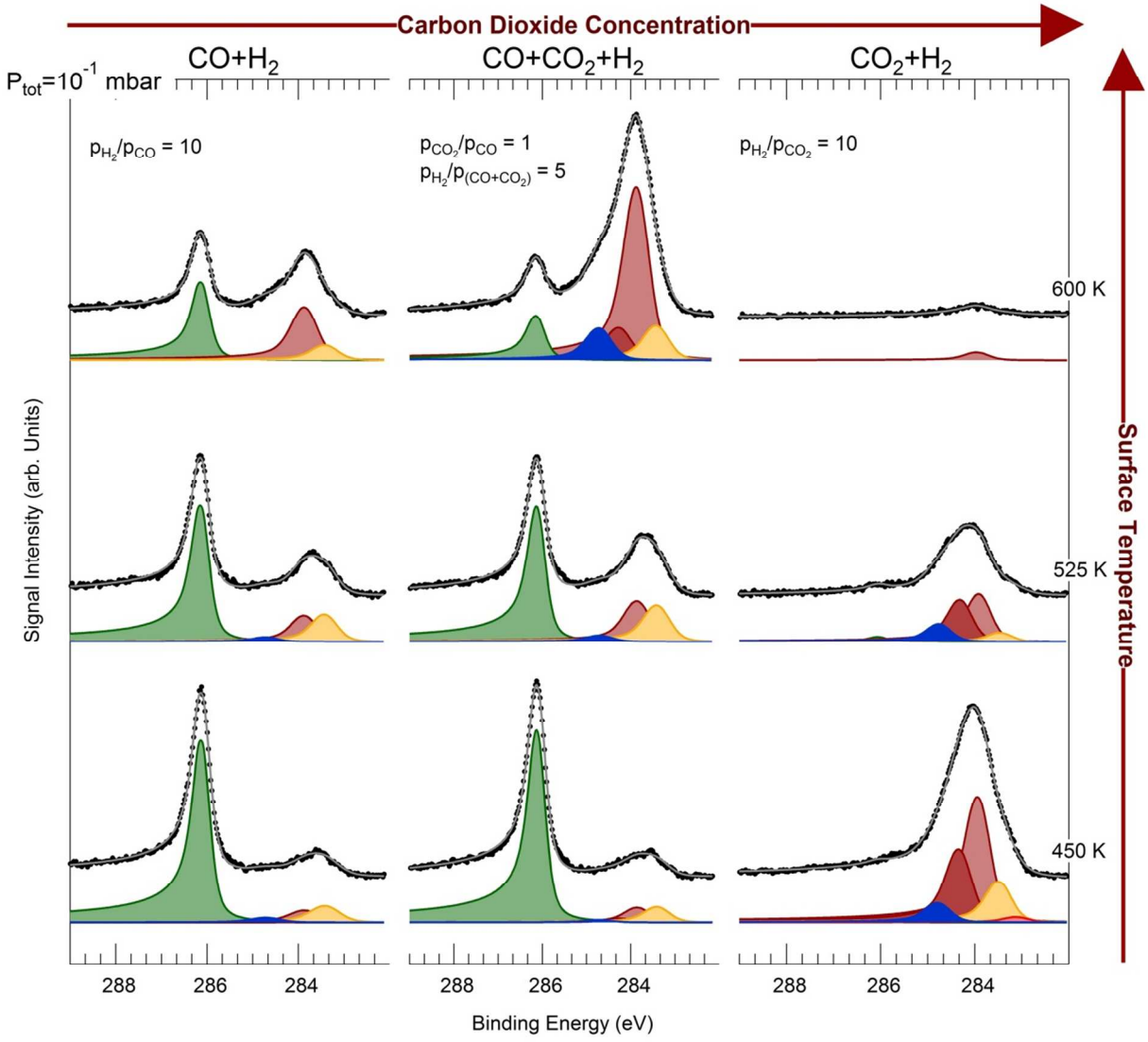
Carbon Dioxide Concentration
CO+H2
CO+CO2+H2
CO2+H2
Ptot=10-1 mbar
pH2/pCO = 10
pCO2/pCO = 1
pH2/p(CO+CO2) = 5
pH2/pCO2 = 10
600 K
525 K
450 K
Signal Intensity (arb. Units)
Surface Temperature
288
286
284
Binding Energy (eV)

Figure 6.

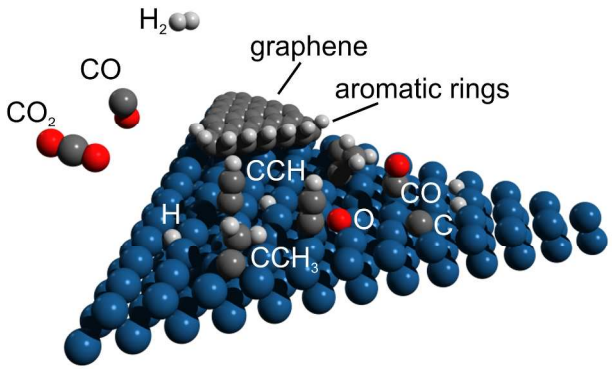

Electronic Supplementary Information

Carbon dioxide reduction on Ir(111): stable hydrocarbon surface species at near-ambient pressure

Manuel Corva,[ab] Zhijing Feng,[ab] Carlo Dri,[ab] Federico Salvador,[b] Paolo Bertoch,[b] Giovanni Comelli,[ab] and Erik Vesselli[*ab]

[a]Physics Department, University of Trieste, via Valerio 2, I-34127 Trieste, Italy

[b]IOM-CNR Laboratorio TASC, Area Science Park, S.S. 14 km 163.5, I-34149 Basovizza (Trieste), Italy

[*]E-mail: vesselli@iom.cnr.it

Discussion of the SFG data fitting procedure

In order to guide the discussion, a selected example is reported in Figure S1 (panel a), where the normalized SFG intensity in the C-O stretching region obtained upon exposure of the Ir(111) surface to 10^{-1} mbar CO_2 is reported. At this point, we thoroughly discuss different possible approaches to the visualization of the data fitting results. Going into further detail, the expression for the second-order susceptibility $\chi^{(2)} = \chi^{(2)}_{NRes} + \chi^{(2)}_{Res}$ in Eq. 1 (main paper) can be conveniently rewritten in order to highlight specific quantities of physical and chemical interest. Indeed, the real and imaginary components of the refraction index describe the scattering and absorption properties of a system, respectively, and can be readily obtained for the resonant part:

$$\chi^{(2)}_{Res}(\omega_{IR}) = Re\left[\sum_k \frac{A_k e^{i\varphi_k}}{\omega_{IR}-\omega_k+i\Gamma_k}\right] + i\, Im\left[\sum_k \frac{A_k e^{i\varphi_k}}{\omega_{IR}-\omega_k+i\Gamma_k}\right] \quad \text{(Eq. S1)}$$

and separately represented in an amplitude (not intensity) plot (Figure S1, panel b). Alternatively, the real (Figure S1, panel c) and imaginary (panel d) amplitudes can be displayed for each k^{th} resonance separately

$$\chi^{(2)}_{Res,k}(\omega_{IR}) = Re\left[\chi^{(2)}_{Res,k}\right] + i\, Im\left[\chi^{(2)}_{Res,k}\right] = Re\left[\frac{A_k e^{i\varphi_k}}{\omega_{IR}-\omega_k+i\Gamma_k}\right] + i\, Im\left[\frac{A_k e^{i\varphi_k}}{\omega_{IR}-\omega_k+i\Gamma_k}\right] \quad \text{(Eq. S2)}$$

thus representing the individual contributions to the resonant amplitudes. The above plotting choices yield alternative visualization possibilities of the information determined with the data least-square fitting procedure and allow speculating about the signal amplitudes.[1] It is indeed known that if N resonances are present in an SFG spectrum, up to 2^N equivalent sets of parameters can be obtained upon data fitting according to Eq. 1.[2,3] This occurs since we actually measure intensities and not amplitudes. In order to unequivocally determine the real and imaginary components of the resonant susceptibility, phase-sensitive SFG spectroscopy should be exploited.[3] Since this is not our case, we here propose and adopt throughout the manuscript a plot of the deconvoluted intensities (not amplitudes) contributing to the effective SFG signal (Figure S1, panel e), thereby avoiding to speculate about amplitudes, but providing visual information about the contribution of each resonance to the overall intensity. For each k^{th} component we therefore display, coherently with the experimental and best fit SFG intensity curves, the following function

$$I_{SFG,k}(\omega_{IR}) \sim \left|A_{NRes} + \frac{A_k e^{i\Delta\varphi_k}}{\omega_{IR}-\omega_k+i\Gamma_k}\right|^2 \qquad \text{(Eq. S3)}$$

This intensity expression accounts for the interference of each of the resonances with the non-resonant background, while interference among different resonances is not represented. The latter, indeed, is already visualized in the fitting curves according to Eq. 1. With reference to Figure S1, panel (e), the intensity curves are color-filled with respect to the non-resonant background, represented by the horizontal dashed line. The vertical dashed lines show the actual positions of the resonances (ω_1 = 2071 cm^{-1}; ω_2 =2080 cm^{-1}) as from the data fitting procedure.

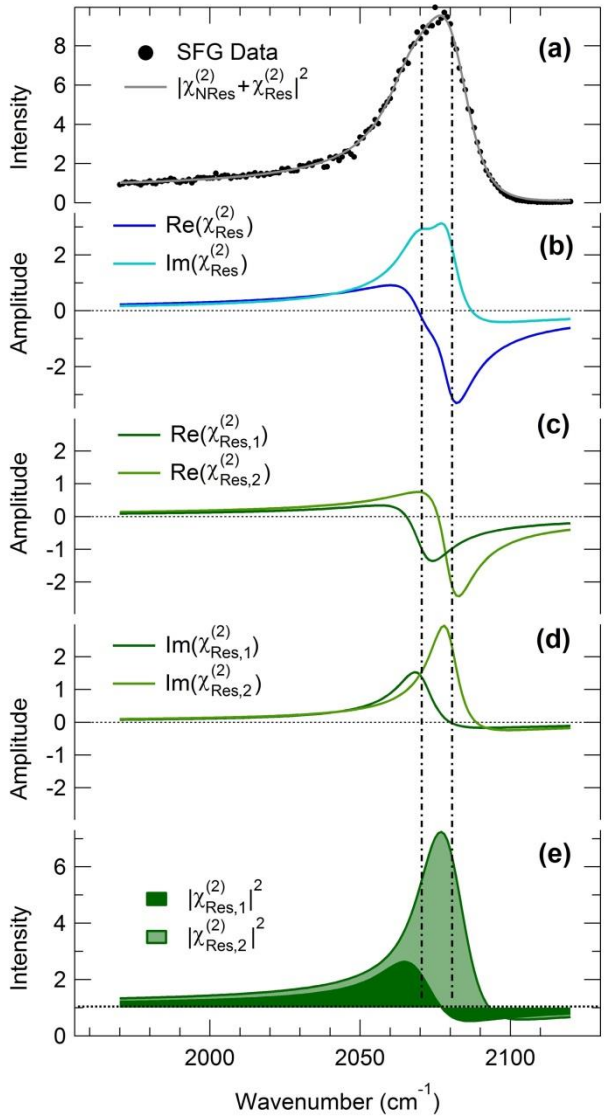

Figure S1. Analysis and interpretation of SFG data: (a) SFG intensity spectrum in the C-O stretching region upon exposure of Ir(111) to CO_2 (dots) and best-fit (grey line) with the function of Eq. 1; as obtained from the least-square fit of the data, (b) shows the amplitude of the real and imaginary parts of the resonant susceptibility (Eq. S1), (c) shows the amplitude of the real part of the resonant susceptibility for each resonance (Eq. S2), (d) shows the amplitude of

the imaginary part of the resonant susceptibility for each resonance (Eq. S2), (e) shows the intensity for each resonance (Eq. S3), color-filled with respect to the non-resonant background (horizontal dashed line); vertical dashed lines show the position of the resonances ω_1 and ω_2 as from the data fitting procedure; amplitude and intensity values (y axis) are in arbitrary units.

We reserve a dedicated discussion to the SFG data fitting procedure adopted for the C-H stretching region, where several features were observed and could be resolved after a careful analysis. In particular, the features at 3000 ± 9 and 3035 ± 6 cm^{-1} (cyan and light blue in Figures S2 and S3) may be attributed at first glance to a single vibrational mode with a dispersive lineshape, in analogy to the peak at 2904 ± 3 cm^{-1} (dark red curve in Figure S2), i.e. in phase quadrature with respect to the non-resonant background.

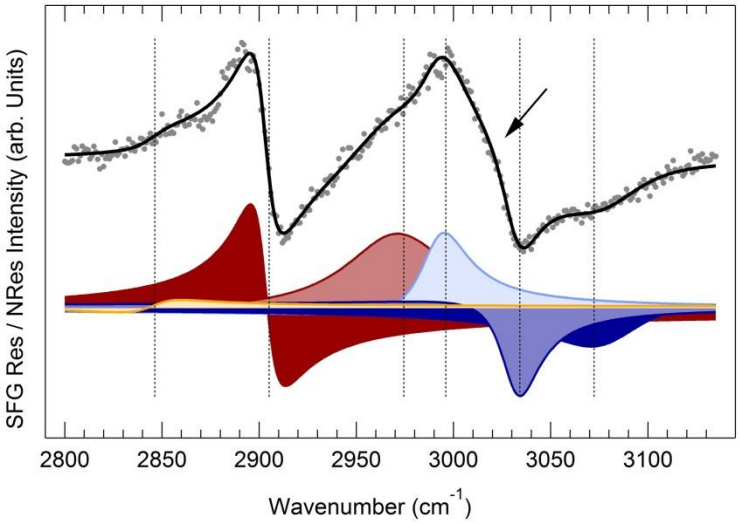

Figure S2. Deconvolution of the C-H stretching region: selected example. The arrow indicates an evident "knee" in the spectrum requiring two distinct peaks to reproduce the data, instead of a single dispersive lineshape. Vertical dashed lines indicate the line-positions.

However, the presence of an evident "knee" in the spectrum (arrow in Figure S2) indicates that two distinct peaks are needed to properly describe the data in that energy region. Indeed, a single dispersive lineshape yields a structured residual and a high chi-value in the least-square fitting analysis. Only with the introduction of two peaks with almost opposite phase the experimental data could be properly reproduced.

Full IR-Vis SFG data set in the C-H stretching region for the carbon dioxide reduction reaction.

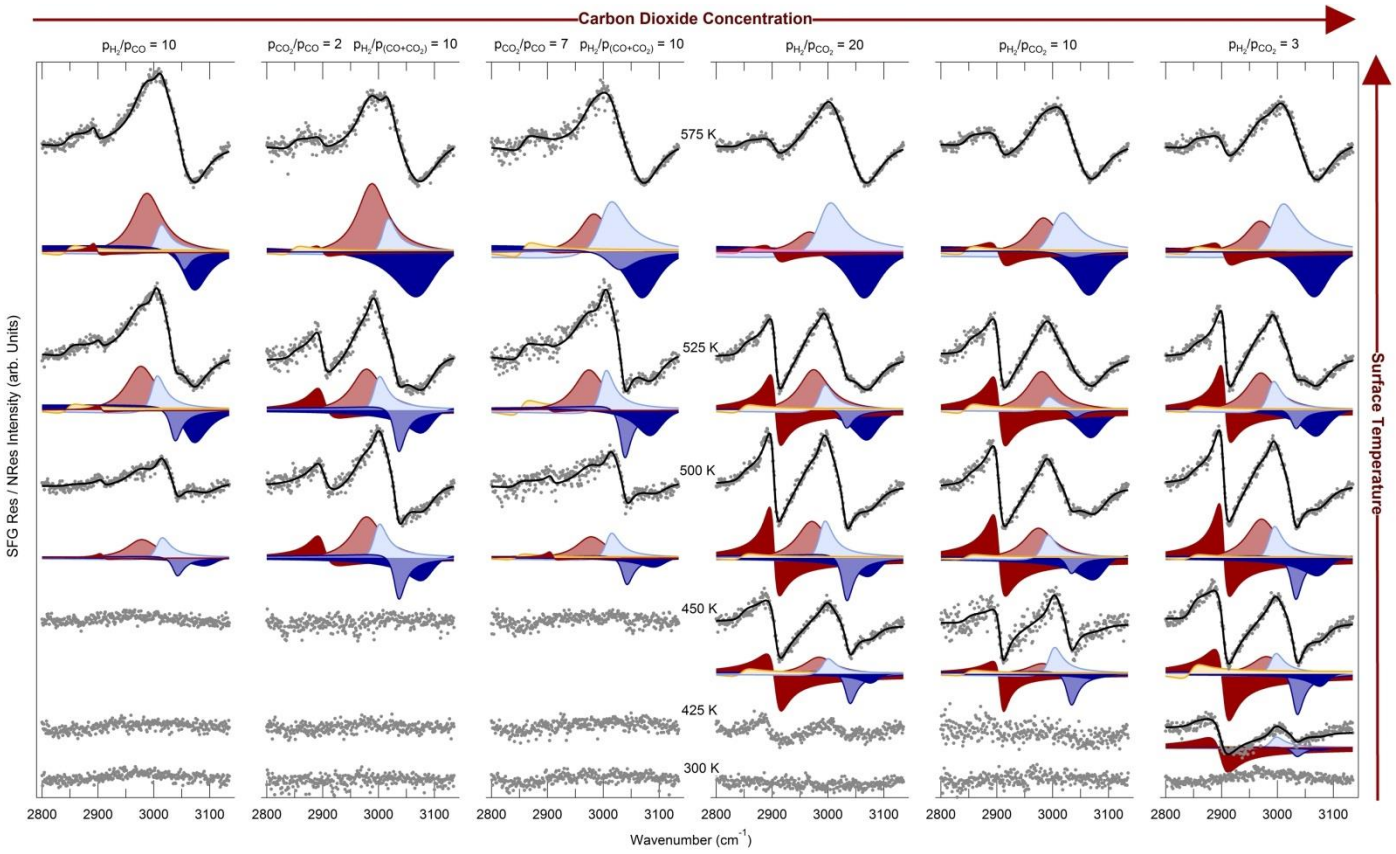

Figure S3. IR-Vis SFG spectra in the C-H stretch region obtained upon annealing the Ir(111) surface exposed to different reactants' partial pressures at 10^{-1} mbar. Data (grey dots) and the results of the least square fitting (black curves) are shown. Colored curves represent deconvoluted intensity modulations with respect to the non-resonant background. [λ_{Vis} = 532 nm; p-p-p polarization]

Fitting parameters of the IR-Vis Spectra (selected representative spectra).

The best fitting parameters' values obtained from the least-square analysis of the SFG data according to the function described in the text are reported in the following tables (Tables S1-S3). While phase and lifetime parameters were obtained from a global fit of the data and were therefore fixed for each data set, the remaining parameters were instead fitted separately for each curve, yielding, in the case of the analysis of the C-O region, error bars of $\Delta\omega$ = 2 cm^{-1}, $\Delta(A_k/A_{NR})/ (A_k/A_{NR})$ = 5 %, and $\Delta\omega_G$ = 2 cm^{-1} respectively. For the C-H region, ranges are given, the exact parameters' values depending on the different reaction conditions.

Experiment	Figure-panel in Main Text	Temperature (K)	IR Resonance (cm^{-1})	Res/NRes Signal ratio	Lifetime (cm^{-1})	Phase (°)	Gaussian Broadening (cm^{-1})
CO_2	1-left	300	2080	26	6	32	4
			2071	16	7	37	4
		500	2060	27	6	32	5
			2050	19	7	37	5
		575	2026	26	24	32	-
CO	1-right	300	2079	43	6	32	6
		500	2064	49	6	32	6
		575	2016	21	21	28	-

Table S1. Best IR-Vis SFG fitting parameters' values for CO_2 and CO adsorption at 10^{-1} mbar on Ir(111), C-O stretching region.

Experiment	Figure-panel in Main Text	Temperature (K)	IR Resonance (cm^{-1})	Res/NRes Signal ratio	Lifetime (cm^{-1})	Phase (°)	Gaussian Broadening (cm^{-1})
H_2+CO	3-left	300	2083	53	6	32	4
		450	2072	55	6	32	4
		525	2033	13	6	32	6
			2019	4.9	7	37	6
H_2+CO_2+CO	3-center	300	2079	31	6	32	5
			2069	12	7	37	5
		450	2067	34	6	32	5
			2054	11	7	37	5
		500	2038	24	6	32	10
			2016	4	7	37	10
H_2+ CO_2	3-right	300	2077	30	6	32	4
			2069	19	7	37	4
		450	2039	32	6	32	7
			2011	2.6	7	37	7

Table S2. Best IR-Vis SFG fitting parameters' values for the reduction experiments at 10^{-1} mbar on Ir(111), C-O stretching region.

IR Resonance Range (cm^{-1})	Res/NRes Signal ratio	Lifetime (cm^{-1})	Phase Range (°)
2845 ± 3	0.0 - 1.1	16	185
2904 ± 3	0.0 - 4.6	11 ± 3	357 ± 18
2976 ± 6	0.0 - 9.6	33	265
3000 ± 9	0.0 - 7.1	18 ± 6	240
3035 ± 6	0.0 - 3.3	16 ± 7	68
3078 ± 10	0.0 - 10.5	31 ± 6	107 ± 18

Table S3. Best IR-Vis SFG fitting parameters' values (ranges, values depending on reaction conditions) for the reduction experiments at 10^{-1} mbar on Ir(111), C-H stretching region.

Ethylene adsorption and dissociation on Ir(111) monitored by IR-Vis SFG.

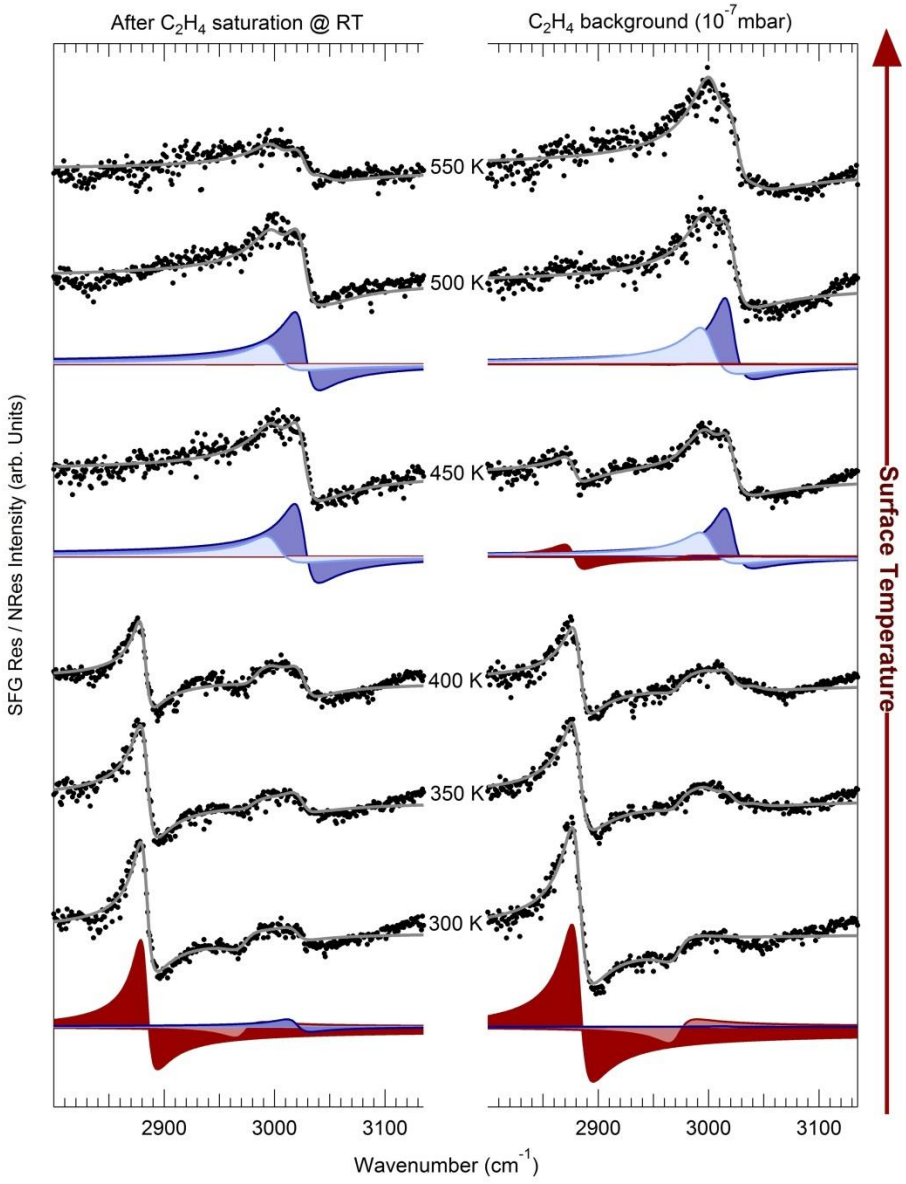

Figure S4. IR-Vis SFG spectra in the C-H stretch region obtained upon annealing the Ir(111) surface after ethylene saturation at RT (left) and in constant ethylene background (right). Data (grey dots) and the results of the least square fitting (black curves) are shown. In selected cases, colored curves represent deconvoluted intensity modulations with respect to the non-resonant background. [λ_{Vis} = 532 nm; p-p-p polarization]

Upon exposure to ethylene of the Ir(111) surface, four main spectral features can be identified in the C-H stretch region at 2880 ± 3, 2975 ± 5, 3002 ± 2, and 3023 ± 3 cm^{-1}. This chemical treatment is widely used to grow a well ordered, almost free standing, graphene sheet

on this surface under UHV conditions. According to the literature,[4] on the basis of high-energy resolution XPS data, the main intermediate present on the surface in the RT - 400 K temperature interval can be identified with ethylidyne (CCH_3), while at higher temperature two non-equivalent ethynyl species (CCH) are reported to be present up to the complete dehydrogenation of the layer occurring at about 700 K, yielding formation of carbon and progressive networking to form graphene. In HREELS spectra a broad feature in the 2940-2960 cm^{-1} range is obtained upon adsorption and decomposition of ethylene or acetylene on Ir(111) and is ascribed to the asymmetric stretching mode of the methyl group of an ethylidyne intermediate.[5] On Pt(111) the same mode is observed at 2939 cm^{-1}.[6] Analogously, on platinum and palladium single crystal terminations the symmetric mode of ethylidyne is observed (by means of SFG, FT-IRAS, and RAIRS) in the 2870-2890 cm^{-1} range.[6–10]

On the basis of these data, we conclude that the two low energy features that we observe below 400 K (red curves) can be ascribed to the symmetric ($\omega = 2880 \pm 3$ cm^{-1}, $\Delta\varphi = 355 \pm 5°$) and antisymmetric ($\omega = 2975 \pm 5$ cm^{-1}, $\Delta\varphi = 155 \pm 20°$) stretching modes of the methyl groups of adsorbed ethylidyne, respectively. The other two features at higher energy (blue curves; $\omega = 3002 \pm 2$ cm^{-1}, $\Delta\varphi = 330 \pm 5°$; $\omega = 3023 \pm 3$ cm^{-1}, $\Delta\varphi = 340 \pm 10°$) are instead due to the stretching of non-equivalent ethynyl species, according to the photoelectron spectroscopy assignment,[4] and on the basis of the vibrational fingerprint of ethynyl intermediates previously observed on Ir(111) and Pt(111) surfaces.[5,6] It is also to be noted that a broad feature (right panel, not fitted) develops progressively at the high energy side of the spectrum with increasing temperature, appearing as a depression in the spectra and shifting from 3040 to 3080 cm^{-1} while heating. This pattern is present up to 700 K (not shown), when complete dehydrogenation of the surface occurs and, as reported in the literature, dome-shaped carbon nanoislands develop as intermediates between carbidic clusters and quasi-free standing graphene.[11]

References

1 M. Ito, H. Noguchi, K. Ikeda and K. Uosaki, *Phys. Chem. Chem. Phys.*, 2010, **12**, 3156.

2 B. Busson and A. Tadjeddine, *J. Phys. Chem. C*, 2009, **113**, 21895–21902.

3 Y. R. Shen, *Annu. Rev. Phys. Chem.*, 2013, **64**, 129–150.

4 S. Lizzit and A. Baraldi, *Catal. Today*, 2010, **154**, 68–74.

5 T. S. Marinova and K. L. Kostov, *Surf. Sci.*, 1987, 181, 573–585.

6 R. Deng, E. Herceg and M. Trenary, *Surf. Sci.*, 2004, **573**, 310–319.

7 M. Morkel, G. Rupprechter and H.-J. Freund, *Surf. Sci.*, 2005, **588**, L209–L219.

8 K. R. McCrea and G. a Somorjai, *J. Mol. Catal. A Chem.*, 2000, 163, 43–53.

9 P. Cremer, C. Stanners, J. W. Niemantsverdriet, Y. R. Shen and G. Somorjai, *Surf. Sci.*, 1995, **328**, 111–118.

10 I. J. Malik, V. K. Agrawal and M. Trenary, *J. Chem. Phys.*, 1988, **89**, 3861–3869.

11 P. Lacovig, M. Pozzo, D. Alfè, P. Vilmercati, A. Baraldi and S. Lizzit, *Phys. Rev. Lett.*, 2009, **103**, 166101.

Graphical abstract - TOC Entry

Stable hydrocarbon surface species in the carbon dioxide hydrogenation reaction were identified on Ir(111) at near-ambient pressure conditions.

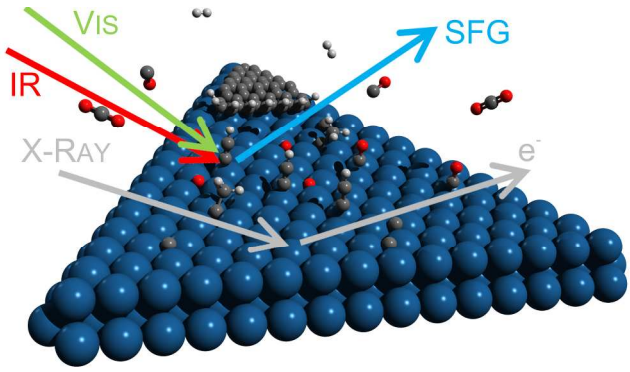

Carbon dioxide reduction on Ir(111): stable hydrocarbon surface species at near-ambient pressure†

Manuel Corva,[ab] Zhijing Feng,[ab] Carlo Dri,[ab] Federico Salvador,[b] Paolo Bertoch,[b] Giovanni Comelli,[ab] and Erik Vesselli[ab]*

[a]Physics Department, University of Trieste, via Valerio 2, I-34127 Trieste, Italy
[b]IOM-CNR Laboratorio TASC, Area Science Park, S.S. 14 km 163.5, I-34149 Basovizza (Trieste), Italy
*E-mail: vesselli@iom.cnr.it
†Electronic supplementary information (ESI) available. See DOI:

Stable hydrocarbon surface species in the carbon dioxide hydrogenation reaction on Ir(111) were identified by means of infrared-visible sum-frequency generation vibrational spectroscopy and X-ray photoelectron spectroscopy at near-ambient pressure conditions (0.1 mbar). Introducing gas phase binary and ternary mixtures of CO_2, CO, and H_2 into the reaction chamber, stable ethylidyne and ethynyl species were found at the metal surface above 425 K, in remarkable analogy with what observed during the ethylene decomposition process yielding graphene. In addition, for increasing temperature (up to 600 K depending on the reaction conditions), vibrational and electronic spectroscopic fingerprints appeared that could be attributed to the nucleation of aromatic hydrocarbons at the edge of metastable graphenic clusters interacting with the metal surface.

1 Introduction

The catalytic reduction of carbon dioxide to generate useful chemicals like *e.g.* methanol, urea, formic acid, and dimethylcarbonate is a possible route to handle and recycle at least a part of this

waste gas, in order to deal with greenhouse emissions produced by the massive use of fossil fuels.[1–4] Many approaches are investigated, involving both homo- and hetero-geneous catalytic environments, electro-catalytic systems, and solar energy harvesting devices, with a particular effort in the quest for catalysts able to mimic the photosynthetic organic synthesis processes driven in nature by visible light.[2,5] In particular, Ir has recently been considered for the catalytic hydrogenation of carbon dioxide in pincer complexes in aqueous solutions, yielding unprecedented turnover numbers towards the synthesis of formic acid via a formate surface species.[3] Moving to model systems and to atomic-level insight, the Ir(111) termination has been largely investigated in Ultra-High Vacuum (UHV) due to its catalytic activity towards the sequential dehydrogenation of hydrocarbons, with particular focus on acetylene and ethylene.[6–9] A progressive carbon networking process occurs, yielding the formation of a well-ordered, almost perfect and free-standing graphene sheet.[10–12] Stable surface species in the hydrocarbon dehydrogenation process have been identified with both vibrational and electronic spectroscopies under UHV conditions, depending on the reaction temperature. In particular, for increasing temperature, ethylidene ($CHCH_3$), ethylidyne (CCH_3), and ethynyl (CCH) species have been observed, the latter being stable up to the complete dehydrogenation of the surface, occurring above 700 K.[6–9] Analogously, formate, methoxy, and acetate stable surface species are detected upon ethanol and methanol thermal decomposition.[13,14] In this framework, however, insight at reaction conditions closer to ambient pressure is still lacking due to the well-known instrumental pressure gap. In addition, almost no information is available about the interaction of carbon dioxide with Ir due to the low molecule-Ir interaction energy,[4] at variance with other metals like Ni that can activate CO_2 through a consistent charge transfer.[15,16] Recent studies on the Ni(110) surface under near-ambient pressure (NAP) reaction conditions have unveiled important

mechanisms involved in the carbon dioxide reduction process, yielding insight into the role of the surface oxidation state and of graphene and carbide domains.[17] When reacting with hydrogen, CO_2 is found to convert to a stable bi-dentate formate species,[4,18] while other more energetically convenient pathways involve an unstable hydrocarboxyl intermediate.[19] To our knowledge, there is no analogous data available about the carbon dioxide activation and reduction process on iridium surfaces, aiming at identifying stable intermediates and possible reaction pathways, either under UHV or at pressures closer to applicative conditions.[4] On the (110) termination of iridium, CO_2 is indeed only weekly bound in a physisorbed state in UHV and readily desorbs when produced by the reaction of carbon monoxide with pre-adsorbed oxygen.[4,20] Motivated by the above considerations, we present here the results obtained at 10^{-1} mbar by coupling Near-Ambient Pressure X-ray Photoelectron Spectroscopy (NAP-XPS) with the powerful approach of Infrared-Visible Sum-Frequency Generation (IR-Vis SFG) vibrational spectroscopy. The latter technique is indeed intrinsically sensitive to interfaces and allows bridging the pressure gap issues, thus providing insight into the catalyst's surface during the reaction with the gas phase.[21,22] Data were collected with the aim of investigating the interaction of carbon monoxide, carbon dioxide, and hydrogen with the Ir(111) single crystal termination as a function of temperature *in situ* and *in operando* conditions. Repeated measurements were performed, starting each time from a clean Ir surface, in order to ensure reproducibility. Thanks to a comparison of the spectroscopic results with previous literature data, we are able to identify stable hydrocarbon species, remarkably including the ethylidene and ethynyl molecules also present during the acetylene and ethylene dehydrogenation processes.

2 Methods

2.1 SFG Experiments.

A novel experimental setup to study catalytically active heterogeneous phases *in situ* and *in operando*, exploiting IR-Vis SFG,[23] has been commissioned at the Physics Department of the University of Trieste. An UHV preparation chamber (base pressure 5×10^{-11} mbar) equipped with standard sample preparation and characterization instruments (sample fast entry-lock, ion gun, LEED optics, gas line, evaporator, and quartz micro-balance for the deposition of molecules, metallic clusters, and thin film growth) is directly connected to a high-pressure cell, where the sample can be transferred without breaking the vacuum. The sample is held by Ta wires and can be resistively heated up to 1300 K in vacuum and up to 800 K in the reactor (K-type thermocouple). The reactor is equipped with a gas handling system in order to control the pressure of the reactants within the 10^{-10}-10^{+3} mbar range. The inlet of the infrared and visible beams, as well as the outlet of the SFG signal, is provided by UHV-compatible BaF_2 windows. The excitation source of the SFG spectrometer (EKSPLA PL2231) consists in a Nd:YAG, diode pumped picosecond IR laser (λ = 1064 nm, E_{max}/pulse = 25 mJ, repetition rate 50 Hz, pulse duration ~30 ps). The radiation enters a harmonics unit where two visible beams (532 nm) are generated (EKSPLA H500 SFG) by means of non-linear crystals (KD_2PO_4). One of the two beams is then mixed with the remaining fraction of the original IR beam in the parametric generator and difference frequency generator unit (EKSPLA PG501/DFG1P, BBO and $AgGaS_2$ crystals) to yield the tunable IR radiation in the 1000-4500 cm^{-1} range with a spectral width better than 6 cm^{-1}. The whole tunable IR laser beam path length is pressurized with N_2 in order to avoid air absorption. The second visible (532 nm) beam is instead directly delivered to the sample surface. The maximum achievable power at the sample is about 30 and 7 MW for the visible and IR beams (pulse energies of about 1 mJ and 200 μJ, respectively). Both incident

beams are linearly polarized (s or p) with 100:1 purity. Moreover, the polarization of the SFG beam can be selected before entering the monochromator (MS2001) and photomultiplier tube (Hamamatsu R7899) detection system. Both data acquisition and instrument control are performed remotely via software interfaces mainly developed in house. In the present study all spectra were collected in the p-p-p polarization configuration (SFG-visible-infrared), at incidence angles of 55° (IR) and 60° (Vis) from the normal to the surface. The dependence of the SFG signal on the azimuthal angle of the Ir(111) surface was not investigated.

The sample was an 8 mm diameter Ir disc (MaTecK GmbH) of 99.99% purity, with <0.1° orientation accuracy and <0.03 μm roughness. For each experiment, the Ir(111) surface was cleaned by standard cycles of Ar^+ sputtering and annealing in UHV, alternated to oxidation cycles ($p = 10^{-7}$ mbar) to remove residual carbon. Surface order was finally checked by LEED, yielding a sharp (1×1) pattern with extremely low background. SFG spectra acquisition time was about 5 min for the C-O and about 45 min for the C-H stretching regions. High-purity reaction gases (3.0 CO, 4.8 CO_2, 5.5 H_2) where injected into the measurement cell through leak valves from aluminum bottles. The background residual pressure was in the low 10^{-10} mbar range.

2.2 Analysis and interpretation of SFG data.

After normalization to the impinging visible and IR intensities, and to the non-resonant background in order to account for sample alignment issues, SFG spectra were analyzed by least-square fitting methods according to the following widely used parametric, effective expression of the non-linear second order susceptibility,[24–27] explicitly accounting for the IR resonances of the IR-Vis transitions and for the non-resonant background:

$$\frac{I_{SFG}(\omega_{IR})}{I_{vis}I_{IR}(\omega_{IR})} \sim \left|\chi^{(2)}\right|^2 = \left|\chi^{(2)}_{NRes} + \chi^{(2)}_{Res}\right|^2 = \left|A_{NRes}e^{i\varphi_{NR}} + \sum_k \frac{A_k e^{i\varphi_k}}{\omega_{IR}-\omega_k+i\Gamma_k}\right|^2 = \left|e^{i\varphi_{NR}}\right|^2 \left|A_{NRes} + \sum_k \frac{A_k e^{i(\varphi_k-\varphi_{NR})}}{\omega_{IR}-\omega_k+i\Gamma_k}\right|^2 = \left|A_{NRes} + \sum_k \frac{A_k e^{i\Delta\varphi_k}}{\omega_{IR}-\omega_k+i\Gamma_k}\right|^2 \qquad \text{(Eq.1)}$$

In this expression A_{NRes} and A_k are therefore real positive numbers and account for the amplitudes of the non-resonant and k^{th}-resonant contributions, respectively, $\Delta\varphi_k=\varphi_k-\varphi_{NR}$ is the phase difference between the k^{th}-resonance and the non-resonant background, ω_k is the energy of the k^{th}-resonance, and Γ_k its Lorentzian broadening related to the resonance lifetime. In order to account for inhomogeneity broadening, in specific cases the resonant part of the lineshape was convoluted with a Gaussian envelope.[28–30] According to previous literature, the Gaussian contribution to the lineshape is easily resolved only if it is comparable with the Lorentzian width. In the specific cases where the latter is predominant, the inhomogeneity contribution is hardly obtained from the fitting procedure and can be neglected to a good approximation.[29] A very detailed and careful analysis of the complex IR-Vis spectra in the C-H region was performed in order to obtain a reliable separation of the different contributions originating from adsorbed species. This was achieved by identifying a unique set of lineshape parameters that allowed optimal fitting of the whole data set. For each SFG spectrum throughout the manuscript we plot the normalized SFG intensity (dots) together with the corresponding best fit (grey lines) according to the above intensity function (Eq. 1), and with the corresponding intensity deconvolution (colors) accounting for the interference of each of the resonances with the non-resonant background. A very detailed description of the SFG data analysis and of the plotted quantities can be found in the Supplementary Information, together with a complete set of best fitting parameters of the full SFG data set.

2.3 NAP-XPS Experiments.

NAP (mbar range) XPS measurements were carried out at the ISISS end-station of the Bessy synchrotron radiation facility at the Helmholtz Zentrum Berlin (Germany).[31] The same Ir(111) single crystal used in the SFG experiments was mounted on a sapphire holder by means of Ta supports and screws. Temperature was measured with a K-type thermocouple, and the sample was heated by laser irradiation of its unpolished back face. After each reactivity experiment, the Ir(111) surface was cleaned by standard cycles of ion sputtering (2.5 keV, Ar^+) and annealing in high vacuum to 750°C, the highest attainable temperature on the sample holder. Absence of contaminants was verified by measuring both selected XPS regions (*e.g.* C 1*s*, O 1*s*) and overview spectra. The flux and pressure of the gases introduced into the reaction cell were handled by means of mass-flow controllers and a motorized valve. The effective partial pressure of the reactants in the measurement chamber may have differed with respect to the nominal values due to the different pumping speeds of different molecules. The ratios we report are therefore target set point values only. Gas purity (always better than 3.0) was checked and monitored using a quadrupole mass spectrometer. The residual background pressure in the measurement chamber was in the 10^{-7} mbar range. Adsorption of the single reactants on the clean Ir(111) surface was performed to exclude effects due to residual contaminants. Absence of the latter was confirmed by means of XPS. NAP-XPS spectra were collected in normal emission geometry and binding energies were calibrated with respect to the Fermi level for each oxygen ($h\nu$ = 650 eV) and carbon ($h\nu$ = 400 eV) core level spectrum, yielding an accuracy in the determination of the binding energy values of ±0.1 eV. After normalization and subtraction of a Shirley background,[32] spectra were analyzed by least-square fitting of the data with Doniach-Šunjić profiles,[33] convoluted with a Gaussian envelope to account for experimental resolution,

inhomogeneity and thermal broadening. A very detailed and careful analysis of the C and O 1*s* core level spectra was performed in order to disentangle the contributions originating from different species. This was achieved by identifying a single set of lineshape parameters that allowed optimal fitting of all the C or O 1*s* spectra. Within this set, in order to reduce the number of degrees of freedom, identical lineshapes were used for groups of similar species. In particular, C 1*s* spectra were fitted with distinct lineshapes for CO, and for C-C and C-H species. The resulting binding energy values were assigned on the basis of literature data as reported in the text.

3 Results and discussion

3.1 CO_2 and CO adsorption.

In order to identify the spectroscopic features related to carbon dioxide adsorption and dissociation, the Ir(111) surface was exposed to 10^{-1} mbar CO_2. In Figure 1 (left panel), IR-Vis SFG spectra of the C-O stretching region collected at selected temperature values are shown. Two distinct features are clearly visible, shifting with temperature from 2080 to 2060 cm^{-1} and from 2070 to 2050 cm^{-1}. The data fitting procedure yields constant phases relative to the non-resonant background of 32° and 37°, respectively. At the highest investigated temperature (575 K), only one feature is present at low energy (2024 cm^{-1}). Details about the SFG fitting parameters of the whole data set can be found in the Supplementary Information (Tables S1-3). In Figure 1 (right panel) we report for comparison also the data obtained upon exposure of the surface to CO under the same experimental conditions. Only one feature is visible in the IR-Vis SFG spectra, shifting progressively for increasing temperature from 2079 to 2063 cm^{-1} and with the same lineshape of the corresponding peak (light green) in the carbon dioxide experiment. The Gaussian broadening is larger with respect to the CO_2 case, reaching values up to 7.7 cm^{-1}. As for

CO_2, also in this case a single, broader feature is found at 575 K, at slightly lower energy (2016 cm^{-1}). We remind that due to the physical origin of the SFG signal, intensities are not necessarily related to surface concentration of the adspecies. Therefore, no conclusions about the surface coverage can be drawn.

On the basis of literature data, it is known that CO adsorption on Ir(111) is non-dissociative at room temperature, yielding a saturation coverage of 0.7 ML (monolayer) with CO molecules adsorbed at on-top Ir sites in a $(3\sqrt{3}\times3\sqrt{3})R30°$-19CO structure. The geometric arrangement of the adsorbed CO molecules is best described within the framework of a Frenkel-Kontorova model, yielding a progressive deviation of the C-O molecular axis from the surface normal with the distance from the center of the CO islands.[34,35] For instance, this nicely accounts for the inhomogeneous broadening observed in our IR-Vis SFG spectra. We further confirm this picture by means of NAP-XPS O and C 1*s* core level spectra collected at 375 K (Figure 2, top panels): apart from small amounts of carbon phases (284 eV) and atomic oxygen (529.9 eV) most likely due to dissociation at surface defects, a single CO species can be observed, yielding spectroscopic peaks at 532.0 and 286.1 eV for the O and C 1*s* core levels, respectively, corresponding to on-top adsorption, in agreement with the literature.[34]

In the case of dissociative adsorption of CO_2, the core level binding energies associated to CO (Figure 2, bottom panel) show a consistent shift to 530.9 eV (O 1*s*) and 286.9 eV (C 1*s*), while an intense feature associated to atomic oxygen appears (529.6 eV, cyan). Complete dissociation is possible, evident from the accumulation of carbon (283.9 eV, red). The reaction $CO_2 \rightarrow CO+O \rightarrow C+2O$ is in agreement with the literature, since carbon monoxide decomposition on Ir(111) is promoted by co-adsorbed oxygen.[36] Above 600 K (not shown), the Ir surface remains oxygen-covered since CO desorbs, while carbon is oxidized and therefore removed.

Only a single sharp peak remains visible at 529.9 eV and no feature is detected in the C 1*s* region. In the vibrational spectra, besides the main C-O stretching peak, a low energy shoulder appears (Figure 1, left panel, dark green). We therefore ascribe the two contributions to CO in on-top configuration (2080-2060 cm^{-1}) and to CO in a modified terminal Ir site close to adsorbed atomic oxygen (2070-2050 cm^{-1}), respectively.[35]

3.2 CO_2 reduction.

The Ir(111) sample was exposed to different reactants mixtures to investigate both the carbon dioxide hydrogenation process and the role of carbon monoxide at a total pressure of 10^{-1} mbar. In Figure 3, IR-Vis SFG spectra in the C-O stretching region are reported for selected relative concentrations of the reactants, going from a pure CO/H_2 (left) to a pure CO_2/H_2 (right) environment. The spectra reveal the presence of CO adsorbed in on-top configuration, with a desorption temperature that is progressively decreasing when raising the CO_2 partial pressure. For a pure CO/H_2 mixture a single feature dominates (light green, left), while a lower energy shoulder (dark green) appears at high temperature in analogy to the pure CO_2 case. When adding CO_2, instead, the peak at low energy is already present at room temperature, indicating an influence of co-adsorbates on adsorbed CO.

Moving to the C-H stretching modes (Figure 4), an interesting set of vibrational features appears, indicating the presence of stable adsorbed hydrocarbon species. For the sake of completeness, a broader range of $CO_2/CO/H_2$ concentration ratios has been investigated (not shown), providing no significant additional insight. The full set of IR-Vis SFG data in the C-H stretching region and the details about the fitting parameters are reported in the Supplementary Information. The data shown in the figure immediately indicate that, when carbon monoxide is

present in the gas mixture of the reactants, hydrocarbon surface species develop at higher temperature. At the lowest investigated H_2/CO_2 ratio (H_2/CO_2 = 3, not shown), C-H bonds can be detected already at 425 K. Deeper insight can be obtained by least-square fitting of the data, as discussed in the following. Starting from the low energy side of the spectra, a feature with very low intensity (yellow) can be identified at 2845 cm^{-1} with a phase of 185°. A more intense peak (dark red) is present at 2904 cm^{-1} (phase -20°/+15°), showing a precise trend as a function of temperature and carbon dioxide concentration: its intensity is indeed higher at low temperature and for high carbon dioxide partial pressures. A very intense and broad feature develops at 2976 cm^{-1} (light red, phase 265°) and other three peaks (different blue grades) appear at 3000, 3035, and 3078 cm^{-1} (phases 240°, 68°, and 107°, respectively). We observe that at first glance a single resonance in phase-quadrature with respect to the non-resonant background, i.e. with a dispersive Fano-like lineshape, may already correctly reproduce the experimental data, instead of the two peaks at 3000 and 3035 cm^{-1} (cyan and light blue in Figure 4), in analogy to the case of the feature at 2904 cm^{-1} (dark red). However, this is not adequate, yielding only poor chi-values and structured residuals in the least-square fitting analysis. A thorough discussion of this issue is presented in the Supplementary Information. At variance with the C-O modes, we do not observe a significant shift of the resonances as a function of the surface temperature. Interestingly, the intensity of the feature at 3078 cm^{-1} grows with temperature at the expense of the intensity of the peak at 3035 cm^{-1}.

NAP-XPS core level spectra collected under the same reaction conditions in the O 1*s* region (not shown) reveal only the presence of adsorbed carbon monoxide, depending on the reaction temperature, while other oxygen-containing species, including atomic oxygen, if present, are below the detection limit. Instead, several spectral contributions appear in the C 1*s*

region (Figure 5). In addition to the peak assigned to carbon monoxide (286.1 eV, green), other peaks appear at lower binding energy, specifically at 283.0, 283.4, 283.9, 284.3, and 284.7 eV. Interestingly and in agreement with what observed with IR-Vis SFG, there is a site competition effect, so that the higher the CO coverage (bottom left part of the graph), the lower the intensities of these contributions, apart from the spectrum at 600 K in pure CO_2/H_2 (top right) where almost no carbon signal is present.

3.3 Identification of stable surface species.

For clarity, the energy positions of the resolved spectroscopic features are reported in Tables 1 and 2 for the vibrational and electronic probes, respectively, together with reference literature data supporting the assignments discussed in the following. The identification of carbon monoxide, originated by both adsorption from the gas phase and/or from the dissociation of carbon dioxide, depending on the reaction conditions, is straightforward when comparing vibrational (peaks at 2013-2083 cm^{-1}) and electronic (peak at 286.1 eV) spectroscopy data with previous literature (Tables 1 and 2, respectively) and with our benchmark experiments (Figures 1 and 2).

Instead, much more effort is needed to interpret and assign the remaining spectroscopic fingerprints. We start from the vibrational features at 2904 and 2976 cm^{-1} (red peaks in Figure 4). On the basis of previous literature data on palladium,[37] iridium,[7] and platinum surfaces,[38,39] the two resonances may be associated with the symmetric and asymmetric stretching modes of the methyl groups of ethylidyne (CCH_3). Indeed, also in the XPS C 1*s* core level spectra the triplet at 283.4, 283.9, and 284.3 eV (Figure 5, red-yellow) well compares with literature data of ethylidyne on Ir(111) obtained from the thermal decomposition of ethylene.[9] The former two peaks are attributed to the two non-equivalent carbon atoms of the molecule, which is bonded to

the surface in upright position through the dehydrogenated termination, while the latter C 1*s* peak is ascribed to the vibrational excitation of the methyl group. To obtain an independent proof of this interpretation, we studied by means of IR-Vis SFG spectroscopy the ethylene dissociation process. In UHV and at temperatures between 300 and 450 K, only two features are clearly visible in the C-H stretching region at 2880 and 2975 cm^{-1}, where, as known from the literature,[9] only ethylidyne is present as a product of the stepwise decomposition of ethylene into ethylidene, ethylidyne, and finally ethynyl species. This further supports our interpretation. By directly comparing the CO_2+CO+H_2 reaction data with the ethylene decomposition experiments on Ir(111) and on the basis of SFG and Fourier Transform Infra-Red (FTIR) measurements on a Pt(111) surface,[40,41] the small peak that we observe at 2845 cm^{-1} (Figure 4, yellow) may be ascribed to the asymmetric CH_3 bend in Fermi resonance with the symmetric C-H stretch.[41] We also observe that if the C-CH_3 bond were perpendicular to the surface, the asymmetric stretch mode would not be visible. This accounts for the poor intensity observed in the spectra obtained upon decomposition of the ethylene layer at variance with the case of the CO_2+CO+H_2 reaction. The intense contribution of this mode to the IR-Vis SFG spectra of the reaction is therefore associated with a deviation of the molecular axis from the upright position due to co-adsorption effects. An alternative, but less supported interpretation of the SFG peak at 2845 cm^{-1} is to assign it to other unsaturated carbon species, namely CH_x, in association with the spectroscopic feature at 283.0 eV in the C 1*s* spectra.[13]

Upon annealing of an ethylidyne layer on Ir(111) above 400 K, dehydrogenation occurs, yielding formation of two non-equivalent ethynyl (CCH) species contributing at 3002 and 3023 cm^{-1} in the vibrational spectra and showing peaks at 283.25 and 283.56 eV in the C 1*s* core level spectra.[9] We therefore attribute to these species the peaks showing up in the reduction

experiments at 3000 and 3035 cm^{-1} (Figure 4, light and intermediate blue). This agrees with the necessity of introducing into the fit procedure two resonances with almost opposite phase, rather than a single dispersive resonance. The phase difference suggests two distinct non-equivalent adsorption geometries for the molecule. Concerning the XPS spectra instead (Figure 5), ethynyl is expected to contribute to the peak at 283.4 eV and is therefore not distinctly resolved in this case.

Finally, with increasing temperature and carbon dioxide concentration (Figure 4, dark blue), a broad feature appears as a depression at 3078 cm^{-1} and is associated with the contribution at 284.7 eV (Figure 5, dark blue) in the C 1*s* core level spectra. While the latter is ascribed to the nucleation of carbide and graphene clusters strongly interacting with the metal surface,[12,42] the vibrational feature, typical of a C-H stretching mode, appears at an energy that is characteristic of aromatic hydrocarbon species.[43] This is compatible with the progressive formation of carbon links, *i.e.* the initial step of a graphene networking process assisted by hydrogen at the periphery of the nucleation islands in agreement with the literature.[44] Further dehydrogenation would therefore yield to the formation of graphenic domes and nucleation islands.[12] However, for the highest studied temperature (600 K) and in absence of carbon monoxide, the high partial pressure of hydrogen in the reaction environment leads to the almost complete reduction and removal of surface carbon (upper right spectrum in Figure 5).

The above findings put in light two significant results. It is indeed observed that stable ethylidyne species can be obtained by a catalytic hydrogenation process at the Ir surface, thus obtaining the same precursor to graphene growth that is generally formed upon thermal decomposition of ethylene adsorbed from the gas phase under UHV conditions. Secondly, the consequent growth of graphene is found to occur via a carbon networking process related with a

progressive formation and dehydrogenation of aromatic species, possibly at the border of the graphene domes. Our work represents therefore a possible spectroscopic evidence and confirmation for what was very recently observed by means of microscopy experiments on both Ir and Ni single crystal surfaces when growing graphene from thermal decomposition of hydrocarbons.[44,45] An important role in the whole reaction mechanism is most likely played by surface and/or subsurface atomic hydrogen species,[46] obtained upon dissociation of gas phase molecular hydrogen from the reactants' background. Our methods did not allow the detection of these species, but, on the basis of literature data obtained under UHV conditions,[47] it is known that atomic hydrogen is still present on the surface up to 450 K on Ir(111). By means of a cartoon representation, we summarize for the sake of clarity in Figure 6 the adsorbed chemical species that we were able to identify at the Ir(111) surface.

4 Conclusions

In conclusion, stable hydrocarbon surface species in the carbon dioxide hydrogenation reaction on Ir(111) were identified by means of infrared-visible sum-frequency generation vibrational spectroscopy and X-ray photoelectron spectroscopy at near-ambient pressure conditions. Ethylidyne and ethynyl species were found at the metal surface above 425 K, in interesting analogy with the ethylene decomposition process yielding graphene. In addition, for increasing temperature (up to 600 K depending on the reaction conditions), vibrational and electronic spectroscopic fingerprints appeared that could be attributed to the nucleation of aromatic hydrocarbons at the periphery of graphenic metastable clusters interacting with the

surface. This provides insight into the graphene growth process that takes place by the progressive extension of graphene islands by means of intermediate aromatic terminations at low temperature.

Acknowledgements

This research was supported by Italian MIUR through the project Futuro in Ricerca FIRB 2010 no. RBFR10J4H7. Consorzio per l'Incremento degli Studi e delle Ricerche dei Dipartimenti di Fisica dell'Università degli Studi di Trieste, Fondazione Casali, and Beneficentia Stiftung are also acknowledged for their contribution in the realization of the SFG setup. Part of the research leading to these results has received funding from the European Community's Seventh Framework Program (FP7/2007-2013) under Grant Agreement No. 226716. We acknowledge the Helmholtz-Zentrum Berlin for provision of synchrotron radiation beamtime at beamline ISISS of BESSY II. The support by Axel Knop-Gericke and Mark Greiner is gratefully acknowledged. Technical support from Andrea Martin (CNR-IOM) and Giovanni Fabian (UniTs), and from the whole administration section of the Physics Department of the University of Trieste is thankfully acknowledged. E.V. thanks K. Föttinger and G. Rupprechter for fruitful discussions about the SFG setup, and N. Seriani for helpful discussions about data interpretation. CNR-IOM is acknowledged for hosting the SFG facility.

REFERENCES

1 C. Song, *Catal. Today*, 2006, **115**, 2–32.

2 C. Wang, Z. Xie, K. E. DeKrafft and W. Lin, *J. Am. Chem. Soc.*, 2011, **133**, 13445–13454.

3 R. Tanaka, M. Yamashita and K. Nozaki, *J. Am. Chem. Soc.*, 2009, **131**, 14168–14169.

4 H.-J. Freund and M. W. Roberts, *Surf. Sci. Rep.*, 1996, **25**, 225–273.

5 J. Barber, *Nat. Struct. Biol.*, 2001, **8**, 577–579.

6 T. S. Marinova and D. V. Chakarov, *Surf. Sci.*, 1987, **192**, 275–282.

7 T. S. Marinova and K. L. Kostov, *Surf. Sci.*, 1987, 181, 573–585.

8 K. L. Kostov and T. S. Marinova, *Surf. Sci.*, 1987, **184**, 359–373.

9 S. Lizzit and A. Baraldi, *Catal. Today*, 2010, **154**, 68–74.

10 B. E. Nieuwenhuys, D. I. Hagen, G. Rovida and G. A. Somorjai, *Surf. Sci.*, 1976, 59, 155–176.

11 J. Wintterlin and M. L. Bocquet, *Surf. Sci.*, 2009, **603**, 1841–1852.

12 P. Lacovig, M. Pozzo, D. Alfè, P. Vilmercati, A. Baraldi and S. Lizzit, *Phys. Rev. Lett.*, 2009, **103**, 166101.

13 C. J. Weststrate, W. Ludwig, J. W. Bakker, A. C. Gluhoi and B. E. Nieuwenhuys, *ChemPhysChem*, 2007, **8**, 932–937.

14 C. J. Weststrate, W. Ludwig, J. W. Bakker, A. C. Gluhoi and B. E. Nieuwenhuys, *J. Phys. Chem. C*, 2007, **111**, 7741–7747.

15 C. Dri, A. Peronio, E. Vesselli, C. Africh, M. Rizzi, A. Baldereschi, M. Peressi and G. Comelli, *Phys. Rev. B*, 2010, **82**, 165403.

16 X. Ding, L. De Rogatis, E. Vesselli, A. Baraldi, G. Comelli, R. Rosei, L. Savio, L. Vattuone, M. Rocca, P. Fornasiero, F. Ancilotto, A. Baldereschi and M. Peressi, *Phys. Rev. B*, 2007, **76**, 195425.

17 E. Monachino, M. Greiner, A. Knop-Gericke, R. Schlögl, C. Dri, E. Vesselli and G. Comelli, *J. Phys. Chem. Lett.*, 2014, **5**, 1929–1934.

18 E. Vesselli, L. De Rogatis, X. Ding, A. Baraldi, L. Savio, L. Vattuone, M. Rocca, P. Fornasiero, M. Peressi, A. Baldereschi, R. Rosei and G. Comelli, *J. Am. Chem. Soc.*, 2008, **130**, 11417–11422.

19 E. Vesselli, M. Rizzi, L. De Rogatis, X. Ding, A. Baraldi, G. Comelli, L. Savio, L. Vattuone, M. Rocca, P. Fornasiero, A. Baldereschi and M. Peressi, *J. Phys. Chem. Lett.*, 2010, **1**, 402–406.

20 T. Matsushima, Y. Ohno and K. Nagai, *Surf. Sci.*, 1990, 239, L561–L564.

21 G. Rupprechter and C. Weilach, *Nano Today*, 2007, 2, 20–29.

22 G. Rupprechter, *Catal. Today*, 2007, **126**, 3–17.

23 Y. R. Shen, *Nature*, 1989, 337, 519–525.

24 B. Busson and A. Tadjeddine, *J. Phys. Chem. C*, 2009, **113**, 21895–21902.

25 F. Vidal and A. Tadjeddine, *Rep. Prog. Phys.*, 2005, **68**, 1095–1127.

26 C. S. Tian and Y. R. Shen, *Surf. Sci. Rep.*, 2014, **69**, 105–131.

27 A. G. Lambert, P. B. Davies and D. J. Neivandt, *Appl. Spectrosc. Rev.*, 2005, **40**, 103–145.

28 J. Y. Huang and Y. R. Shen, *Phys. Rev. A*, 1994, **49**, 3973–3981.

29 L. Velarde and H.-F. Wang, *Phys. Chem. Chem. Phys.*, 2013, **15**, 19970–84.

30 A. L. Mifflin, L. Velarde, J. Ho, B. T. Psciuk, C. F. a. Negre, C. J. Ebben, M. A. Upshur, Z. Lu, B. L. Strick, R. J. Thomson, V. S. Batista, H.-F. Wang and F. M. Geiger, *J. Phys. Chem. A*, 2015, **119**, 1292–1302.

31 A. Knop-Gericke, E. Kleimenov, M. Havecker, R. Blume, D. Teschner, S. Zafeiratos, R. Schlögl, V. Bukhtiyarov, V. V. Kaichev, I. P. Prosvirin, A. Nizovskii, H. Bluhm, A. Barinov, P. Dudin and M. Kiskinova, *Adv. Catal.*, 2009, **52**, 213–272.

32 D. Shirley, *Phys. Rev. B*, 1972, **5**, 4709–4714.

33 S. Doniach and M. Sunjic, *J. Phys. C*, 1970, **3**, 285–291.

34 E. Grånäs, M. Andersen, M. A. Arman, T. Gerber, B. Hammer, J. Schnadt, J. N. Andersen, T. Michely and J. Knudsen, *J. Phys. Chem. C*, 2013, **117**, 16438–16447.

35 J. Lauterbach, R. W. Boyle, M. Schick, W. J. Mitchell, B. Meng and W. H. Weinberg, *Surf. Sci.*, 1996, 366, 228.

36 M. Pan, S. Hoang, J. Gong and C. B. Mullins, *Chem. Commun. (Camb).*, 2009, 7300–7302.

37 M. Morkel, G. Rupprechter and H.-J. Freund, *Surf. Sci.*, 2005, **588**, L209–L219.

38 K. R. McCrea and G. A. Somorjai, *J. Mol. Catal. A Chem.*, 2000, 163, 43–53.

39 R. Deng, E. Herceg and M. Trenary, *Surf. Sci.*, 2004, **573**, 310–319.

40 P. Cremer, C. Stanners, J. W. Niemantsverdriet, Y. R. Shen and G. Somorjai, *Surf. Sci.*, 1995, **328**, 111–118.

41 I. J. Malik, V. K. Agrawal and M. Trenary, *J. Chem. Phys.*, 1988, **89**, 3861–3869.

42 R. Larciprete, S. Fabris, T. Sun, P. Lacovig, A. Baraldi and S. Lizzit, *J. Am. Chem. Soc.*, 2011, **133**, 17315–17321.

43 M. Endlich, S. Gozdzik, N. Néel, A. L. da Rosa, T. Frauenheim, T. O. Wehling and J. Kröger, *J. Chem. Phys.*, 2014, **141**, 184308.

44 L. L. Patera, F. Bianchini, G. Troiano, C. Dri, C. Cepek, M. Peressi, C. Africh and G. Comelli, *Nano Lett.*, 2015, **15**, 56–62.

45 Y. Li, D. Subramaniam, N. Atodiresei, P. Lazić, V. Caciuc, C. Pauly, A. Georgi, C. Busse, M. Liebmann, S. Blügel, M. Pratzer, M. Morgenstern and R. Mazzarello, *Adv. Mater.*, 2013, **25**, 1967–1972.

46 E. Vesselli, J. Schweicher, A. Bundhoo, A. Frennet and N. Kruse, *J. Phys. Chem. C*, 2011, **115**, 1255–1260.

47 D. V. Chakarov and T. S. Marinova, *Surf. Sci.*, 1988, **204**, 147–160.

48 M. Y. Smirnov, V. V. Gorodetskii, A. R. Cholach and D. Y. Zemlyanov, *Surf. Sci.*, 1994,

311, 308–321.

Figures and Tables Captions

Table 1 Energies (cm^{-1}) of the observed vibrational modes, comparison with the literature, and proposed identification of the stable species.

Table 2 C 1*s* core level binding energies (eV), comparison with the literature, and proposed identification of the stable species.

Fig. 1 IR-Vis SFG spectra of Ir(111) in the C-O stretching region collected *in situ* upon exposure of the clean surface to 10^{-1} mbar CO (right panel) and CO_2 (left panel) at selected temperature steps, increasing bottom to top; data (black dots) and the results of the least square fitting (grey curves) are shown; color-filled curves represent deconvoluted intensity modulations with respect to the non-resonant background. [λ_{Vis} = 532 nm; p-p-p polarization]

Fig. 2 NAP-XPS O (left) and C 1*s* (right) core level spectra of Ir(111) collected *in situ* upon exposure of the clean surface to 10^{-1} mbar CO (upper panels) and CO_2 (bottom panels) at 375 K. The deconvolution (color) of the data (black dots) obtained by means of least square fitting (grey curves) is also shown. [hν = 650 (400) eV for oxygen (carbon)]

Fig. 3 IR-Vis SFG spectra of Ir(111) in the C-O stretching region collected *in situ* and *in operando* during the hydrogen reduction of CO (left panel), CO_2 (right panel), and of a mixture of the two (central panel) at a total pressure of 10^{-1} mbar and for progressively increasing temperature (bottom to top); data (black dots) and the results of the least square fitting (grey curves) are shown; color-filled curves represent deconvoluted intensity modulations with respect to the non-resonant background. [λ_{Vis} = 532 nm; p-p-p polarization]

Fig. 4 IR-Vis SFG spectra of Ir(111) in the C-H stretching region collected *in situ* and *in operando* during the hydrogen reduction of CO (left panel), CO_2 (right panel), and of a mixture of the two (central panel) at a total pressure of 10^{-1} mbar and for progressively increasing temperature (from bottom to top); data (black dots) and the results of the least square fitting (grey curves) are shown; color-filled curves represent deconvoluted intensity modulations with respect to the non-resonant background. [λ_{Vis} = 532 nm; p-p-p polarization]

Fig. 5 NAP-XPS C 1*s* core level spectra of Ir(111) during the hydrogen reduction of CO (left panel), CO_2 (right panel), and of a mixture of the two (central panel) at a total pressure of 10^{-1} mbar and for progressively increasing temperature (from bottom to top). The deconvolution (color) of the data (black dots) obtained by means of least square fitting (grey curves) is also shown. [hν =400 eV]

Fig. 6 Cartoon summary of the stable adsorbed species identified at the Ir(111) surface upon hydrogenation of CO and CO_2 at NAP conditions.

Table 1.

This work	Mode	Species	Reference	
2013-2083	C-O stretch	CO (on-top)	2030-2090[35]	Ir
2845	Fermi res.	Ethylidyne (CCH_3)	2795,2857[40,41]	Pt
2904	CH_3 symm. stretch	Ethylidyne (CCH_3)	2870-2890[37,38] 2880*	Pd,Pt Ir
2976	CH_3 asymm. stretch	Ethylidyne (CCH_3)	2940-2960[7,39] 2975*	Ir,Pt
3000,3035	CH stretch	Ethynyl (CCH)	3010-3040[7,39,48] 3002,3023*	Ir,Pt
3078	CH stretch	Aromatic hydrocarbon	3057[43]	Ir

**This work, from ethylene dissociation: see Supplementary Information for details*

Table2.

This work	Species	Reference
283.0	Methylidyne (CH)	283.2[13]
283.4	Ethylidyne (CCH_3)	283.53[9]
	Ethynyl (CCH)	283.25-283.56[9]
283.9	Ethylidyne (CCH_3)	283.93[9]
	Surface carbon	283.77[9]
284.3	Ethylidyne (CCH_3) – vib. exc.	284.32[9]
284.7	Graphene interacting with Ir	284.6[42]
	C atoms at the periphery of graphenic clusters	284.9[12]
286.1	CO	286.2-286.3[14,34]

All literature data refer to the Ir(111) surface

Figure 1.

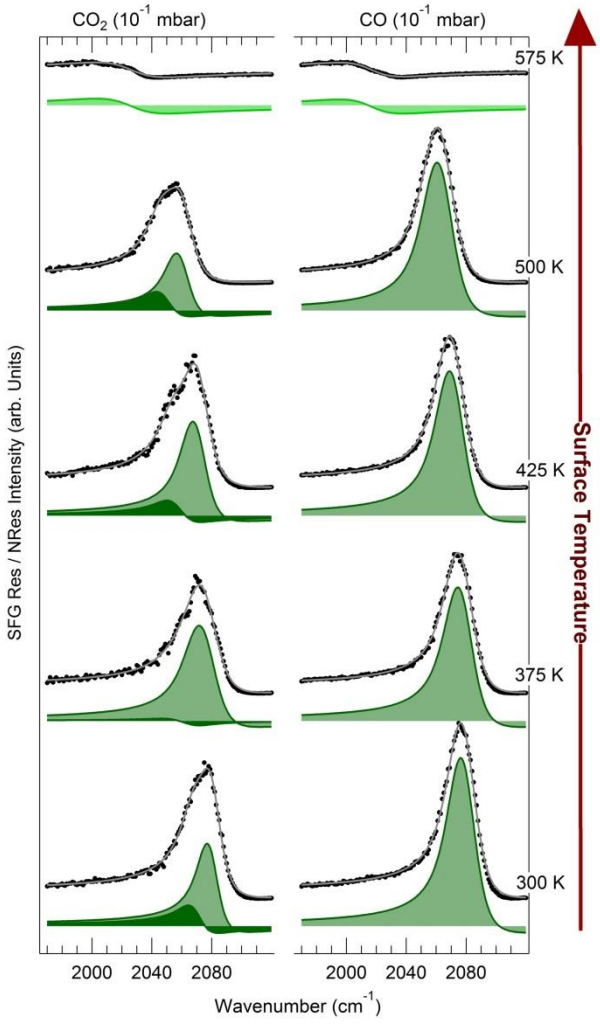
CO2 (10-1 mbar)
CO (10-1 mbar)
575 K
500 K
425 K
375 K
300 K
Surface Temperature
SFG Res / NRes Intensity (arb. Units)
2000 2040 2080
2000 2040 2080
Wavenumber (cm-1)

Figure 2.

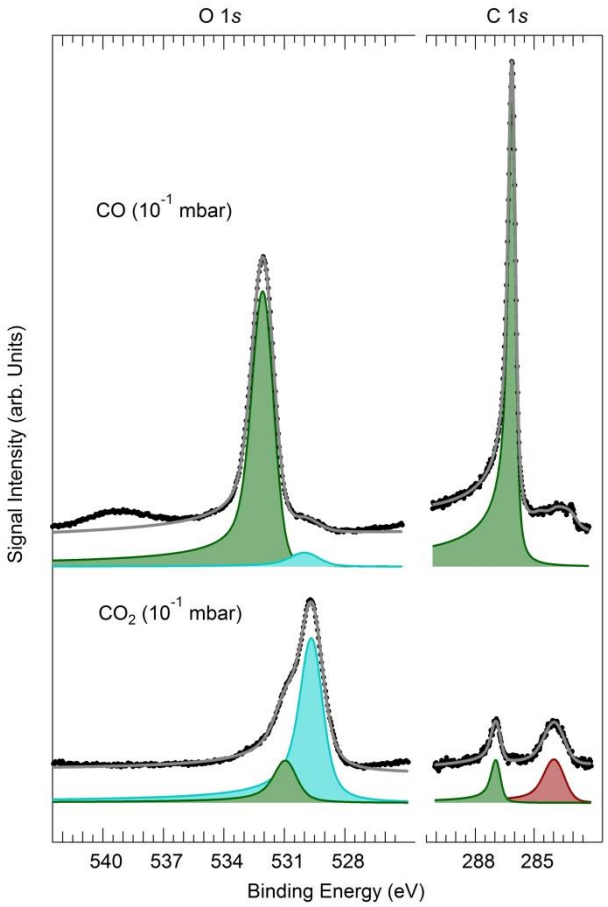
O 1s
C 1s
CO (10^-1 mbar)
CO2 (10^-1 mbar)
Signal Intensity (arb. Units)
540
537
534
531
528
288
285
Binding Energy (eV)

Figure 3.

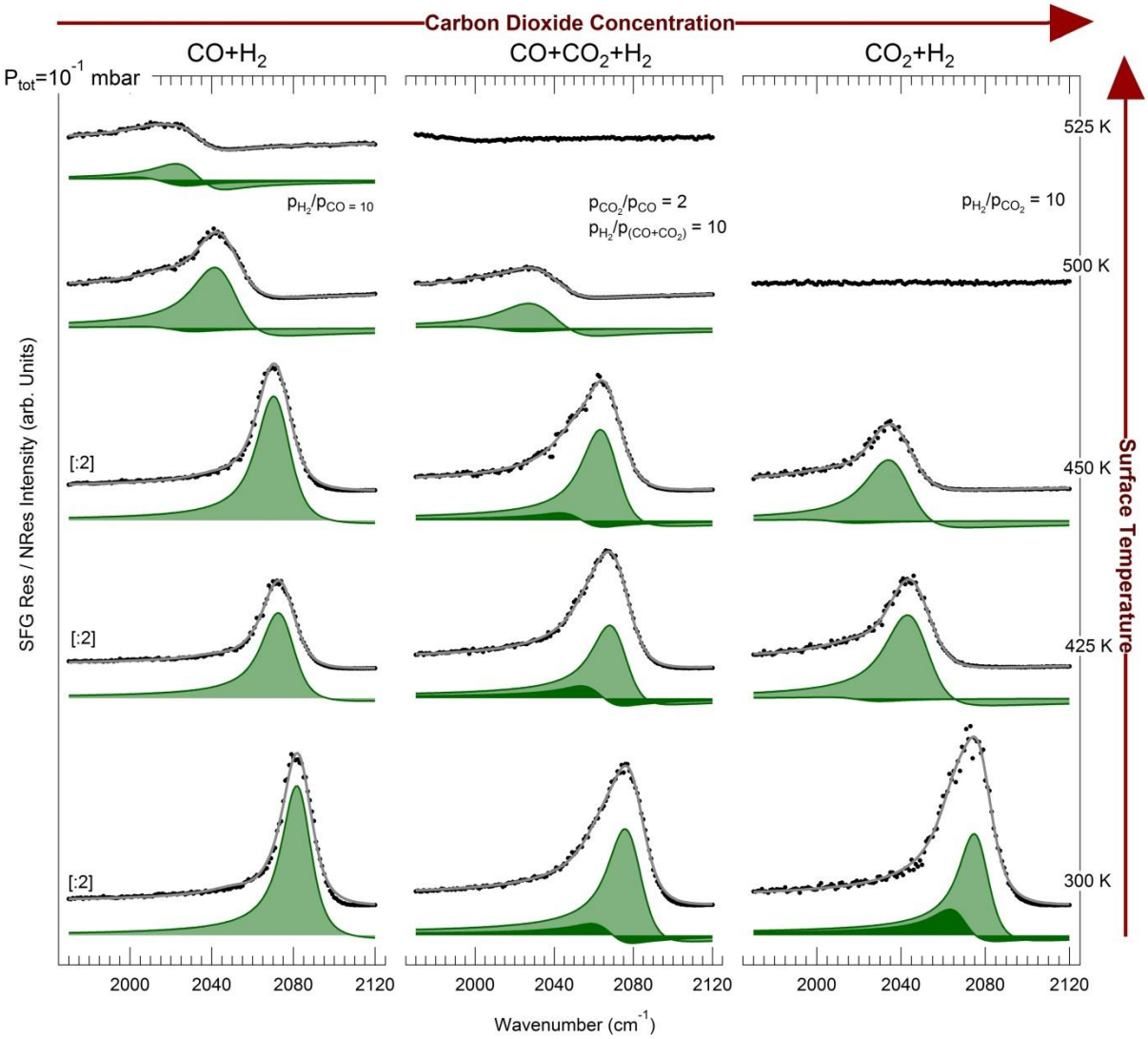
Carbon Dioxide Concentration
CO+H2
CO+CO2+H2
CO2+H2
Ptot=10-1 mbar
525 K
500 K
450 K
425 K
300 K
pH2/pCO = 10
pCO2/pCO = 2
pH2/p(CO+CO2) = 10
pH2/pCO2 = 10
[:2]
[:2]
[:2]
SFG Res / NRes Intensity (arb. Units)
Surface Temperature
2000
2040
2080
2120
Wavenumber (cm-1)

Figure 4.

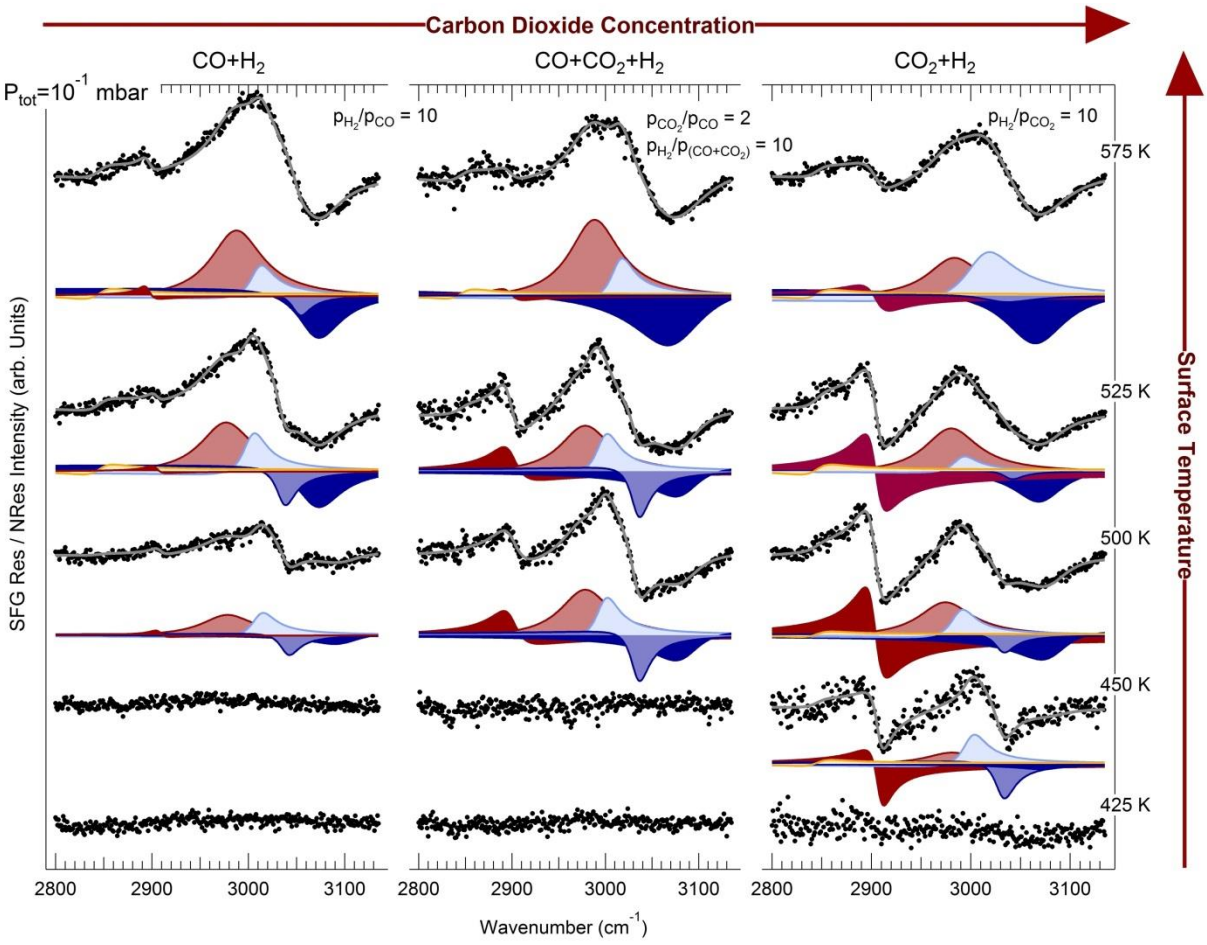
Carbon Dioxide Concentration
CO+H2
CO+CO2+H2
CO2+H2
Ptot=10-1 mbar
pH2/pCO = 10
pCO2/pCO = 2
pH2/p(CO+CO2) = 10
pH2/pCO2 = 10
575 K
525 K
500 K
450 K
425 K
Surface Temperature
SFG Res / NRes Intensity (arb. Units)
2800
2900
3000
3100
Wavenumber (cm-1)

Figure 5.

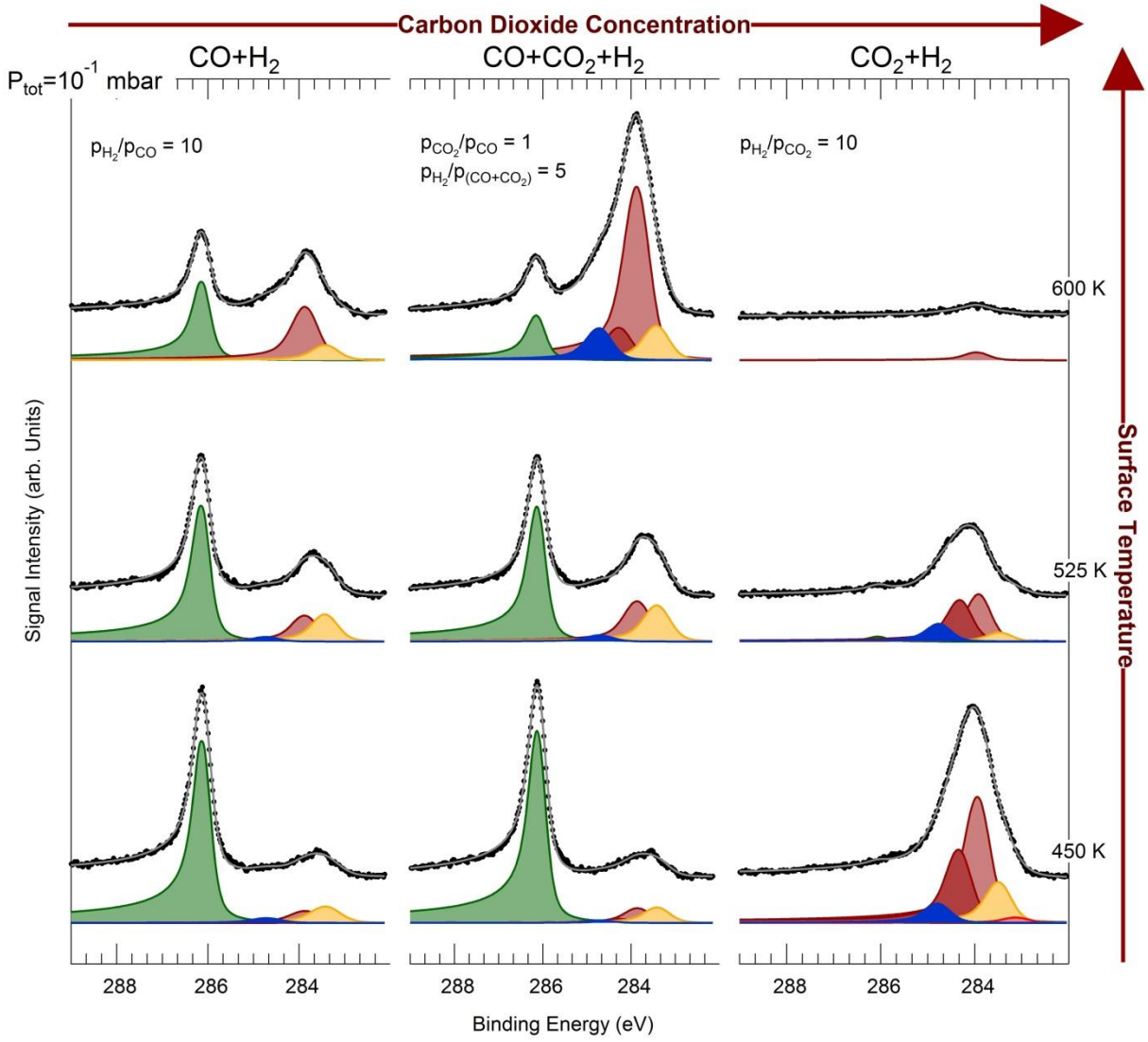
Carbon Dioxide Concentration
CO+H2
CO+CO2+H2
CO2+H2
Ptot=10-1 mbar
pH2/pCO = 10
pCO2/pCO = 1
pH2/p(CO+CO2) = 5
pH2/pCO2 = 10
600 K
525 K
450 K
Surface Temperature
Signal Intensity (arb. Units)
288
286
284
Binding Energy (eV)

Figure 6.

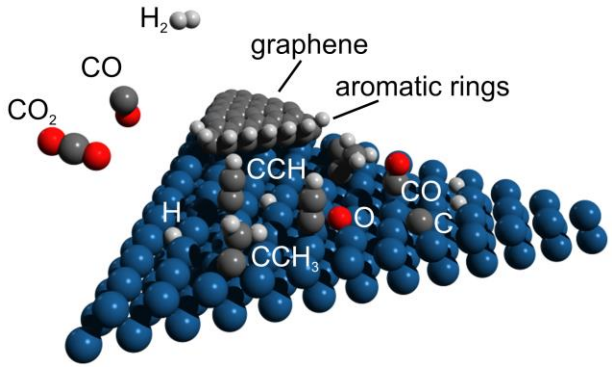

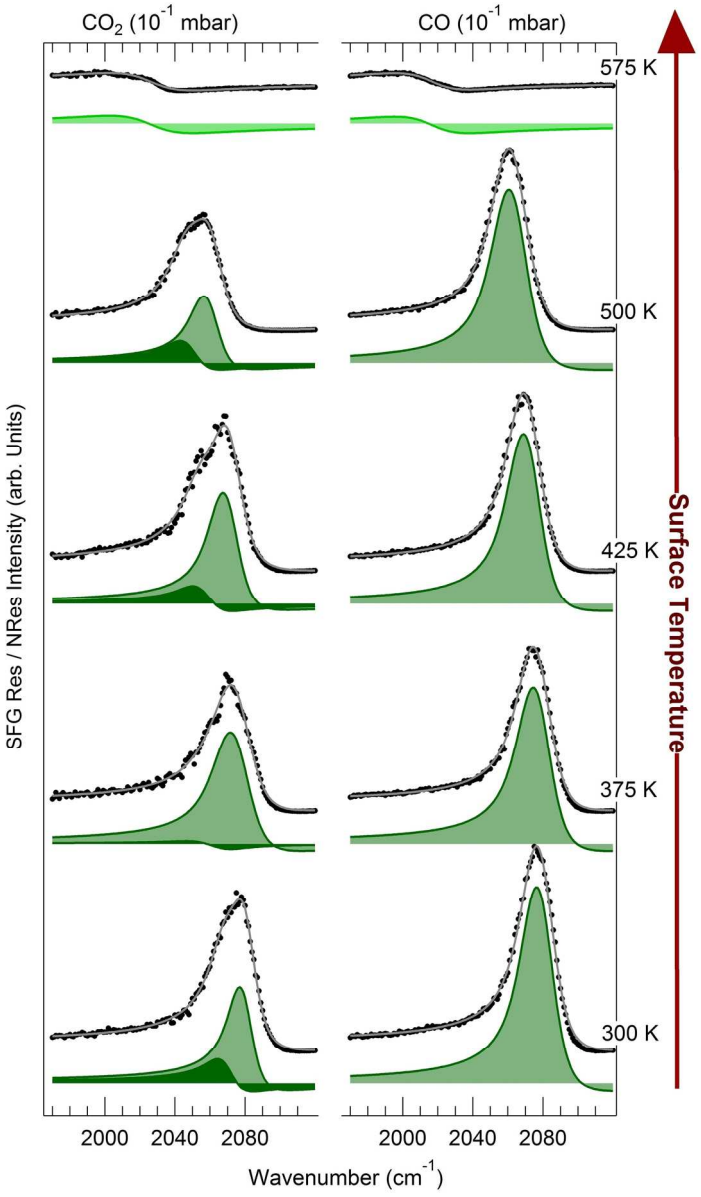

135x229mm (300 x 300 DPI)

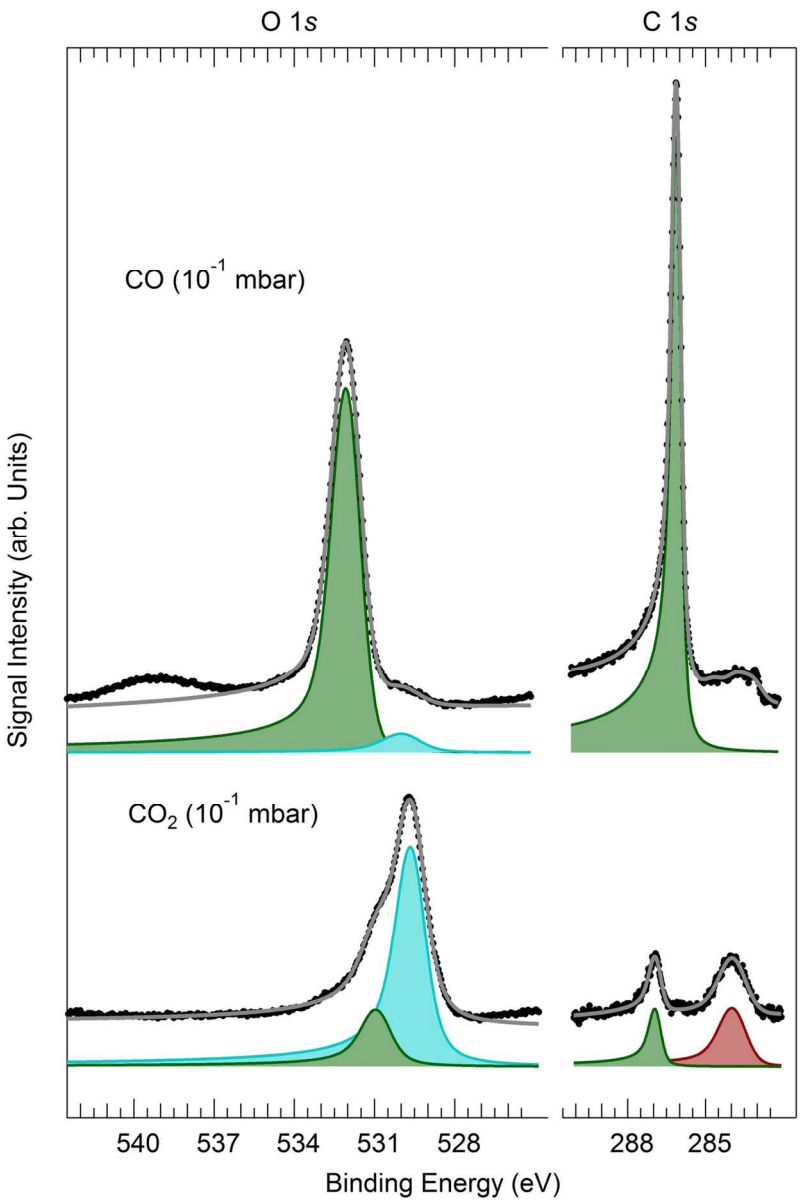

119x178mm (300 x 300 DPI)

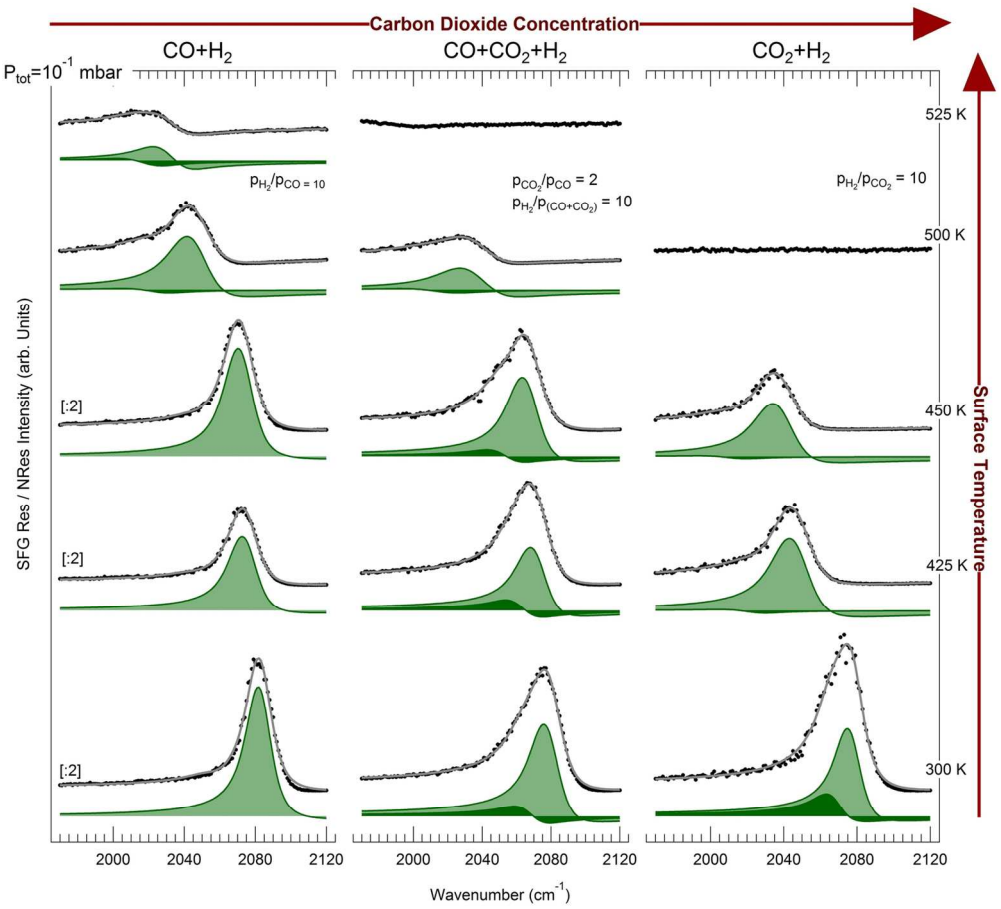

144x130mm (300 x 300 DPI)

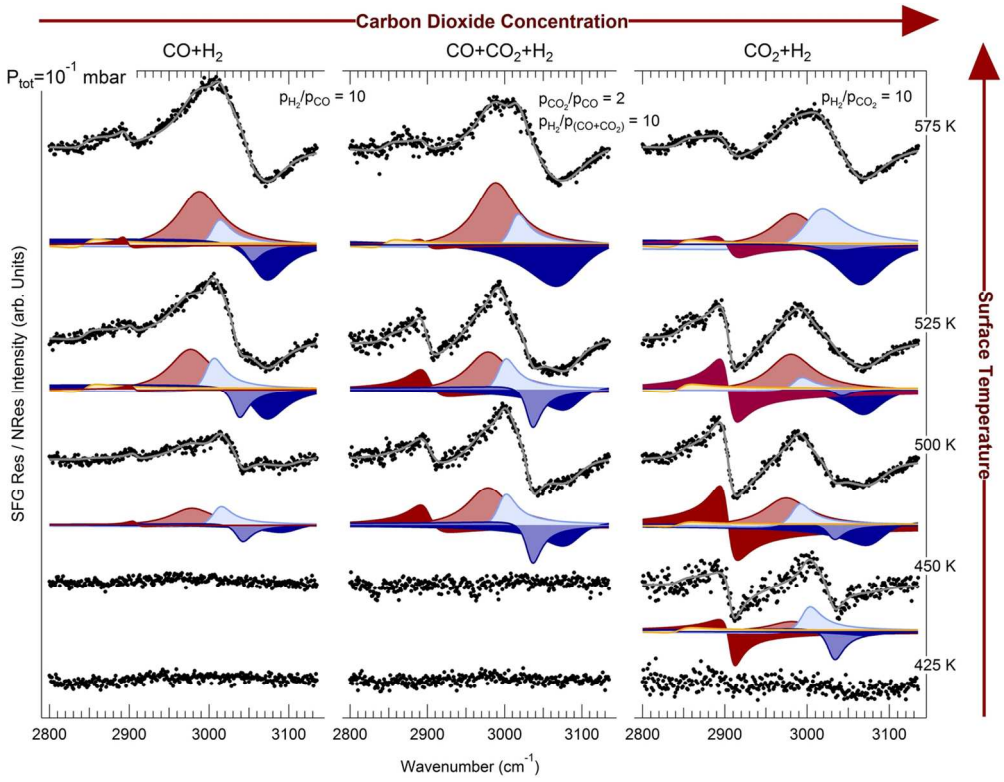

124x96mm (300 x 300 DPI)

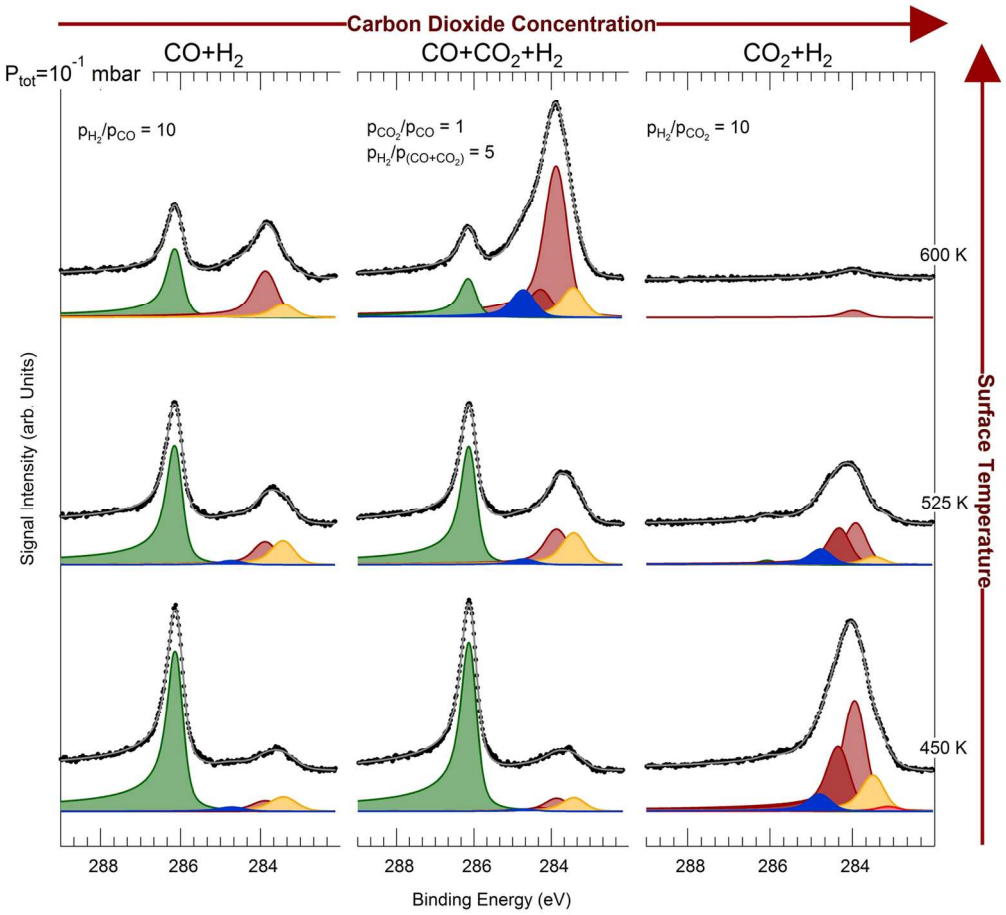

146x133mm (300 x 300 DPI)

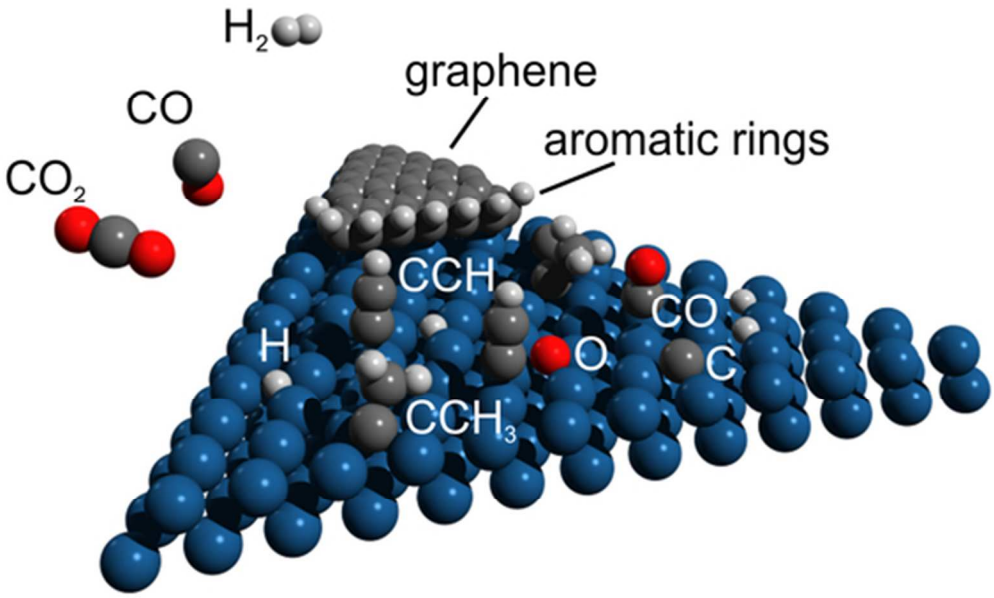

48x28mm (300 x 300 DPI)

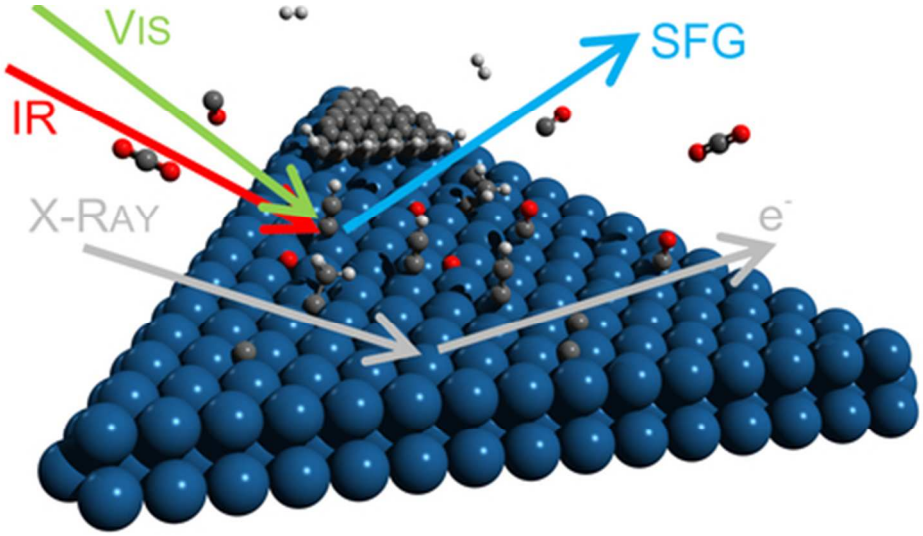

39x22mm (300 x 300 DPI)